
A Measurement of Cosmic Antiproton Flux
at Low Energies
宇宙線反陽子流束の低エネルギー領域における測定
吉村浩司

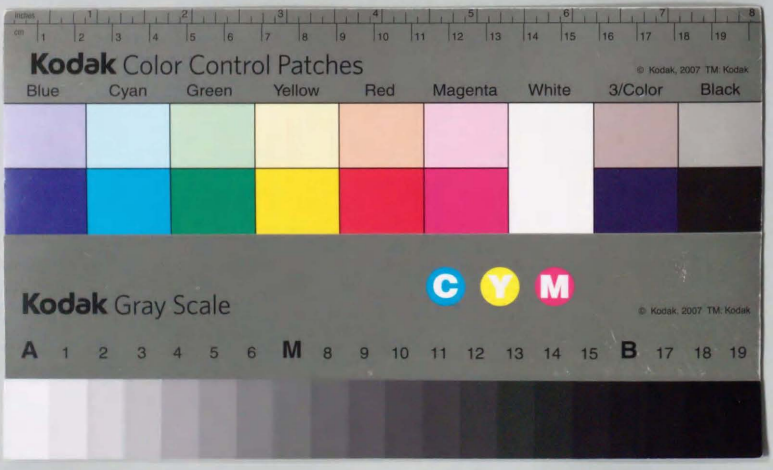
Kodak Color Control Patches
© Kodak, 2007 TM: Kodak
Blue
Cyan
Green
Yellow
Red
Magenta
White
3/Color
Black
Kodak Gray Scale
© Kodak, 2007 TM: Kodak
A 1 2 3 4 5 6 M 8 9 10 11 12 13 14 15 B 17 18 19

A Measurement of Cosmic Antiproton Flux at Low Energies

By
Koji Yoshimura

Department of Physics, Faculty of Science,
University of Tokyo

1994

Abstract

This dissertation analyzes measurements taken in the search for cosmic-ray antiprotons ($\bar{p}$'s) having energies from 175 to 500 MeV at the top of the atmosphere. Data was obtained from a Balloon-borne Experiment with a Superconducting magnet rigidity Spectrometer (BESS). Using '93 flight data, events were selected containing a single good track. Antiprotons were identified by measurements of magnetic rigidity, time of flight, and $\mathrm{d}E/\mathrm{d}X$. The resultant good track quality and sufficient mass spectra led to the observation of four $\bar{p}$'s with an energy between 300 and 500 MeV, being the lowest-energy, cosmic-origin $\bar{p}$'s ever observed. The corresponding $\bar{p}/p$ flux ratio at the top of the atmosphere was found to be $(1.2 \pm 0.65 \pm 0.2) \times 10^{-5}$, where the first and second error values are respectively statistical and systematic errors. Since no $\bar{p}$'s were observed in the energy range between 175 and 300 MeV, this enables establishing a 90% C.L. upper limit flux ratio of 2.9×10^{-5} across the energy range. The obtained $\bar{p}/p$ ratios are compatible with existing upper limits, being the first $\bar{p}/p$ ratio measurements at energies less than 500 MeV.

Acknowledgments

Sincere gratitude is extended to Professor S. Orito for providing me with the great opportunity to join the BESS group and also supporting my associated research. I am particularly grateful to Prof. A. Yamamoto for leading this experiment to a success, and to Prof. M. Nozaki for his overall support.

I also thank my other BESS colleague who helped me perform the present analysis: Dr. T. Yoshida for contributing to the data analysis, Mr. K. Anraku for simulation work, Mr. I. Ueda for calibration of TOF timing, Mr. T. Saeki for z-calibration of the JET chamber, Mr. H. Matsunaga for assistance in coding the track-fitting routine, and Mr. M. Motoki for help in performing the chamber calibration.

I am indebted to Messrs. Y. Makida, K. Tanaka, M. Kimura, and other Magnet Staff Members for their excellent work on the superconducting magnet; and to the following KEK members: Messrs. J. Suzuki, Y. Higashi, Y. Ajima, Y. Kojima, and S. Koizumi, who constructed of the BESS detector.

Furthermore, I express gratitude to Messrs. T. Haga, N. Takimi, H. Honda, and other people who were involved early in this experiment.

Special thanks are due to the National Aeronautics and Space Administration, Goddard Space Flight Center (NASA/GSC) and National Scientific Balloon Facility (NSBF) for providing us the balloon and launch, especially Messrs. J. Ormes, R. Streightmatter, D. Righter, and J. Mitcell.

I gratefully acknowledge helpful suggestions from Prof. J. Nishimura concerning secondary antiprotons in the atmosphere and overall support from Profs. N. Yajima, T. Yamagami, R. Golden, and B. Kimbell.

I further thank Prof. H. Hirabayashi, Ms. C. Tanaka, Ms. K. Nagai, and Ms. S. Tanaka for their hospitality while at KEK, as well as the people in Lynn Lake for their kind hospitality during our stay in Canada.

The presented analysis and simulation were performed on RS/6000 workstations supplied by IBM Japan, Ltd. under their "Partnership Program."

Contents

1 Introduction 1

2 Experimental Apparatus 6
- 2.1 Basic Features . . . 6
- 2.2 Superconducting Solenoidal Magnet . . . 8
- 2.3 JET chamber . . . 10
- 2.4 Inner and Outer Drift Chamber . . . 12
- 2.5 Time of Flight Hodoscope . . . 19
- 2.6 Data Acquisition System . . . 24
  - 2.6.1 Trigger . . . 25
  - 2.6.2 Event Processing with Transputer . . . 31
  - 2.6.3 Data Storage . . . 33
  - 2.6.4 Communication . . . 34
  - 2.6.5 Monitor . . . 34

3 Data Samples 35
- 3.1 Status of BESS '93 Flight . . . 35
- 3.2 Flight Data Sample . . . 35
- 3.3 Data Processing . . . 37
- 3.4 Monte Carlo Simulation Sample . . . 39

4 Detector Performance 42
- 4.1 Measurement Method . . . 42
  - 4.1.1 Rigidity Measurement . . . 42
  - 4.1.2 Time of Flight Measurement . . . 43
  - 4.1.3 $\mathrm{d}E/\mathrm{d}X$ Measurement . . . 45
- 4.2 Event Selection . . . 45
  - 4.2.1 Selection for Good Single Track . . . 46
  - 4.2.2 Track Quality Cut . . . 46
  - 4.2.3 Selection Based on a Quality of the TOF Measurement . . . 47
  - 4.2.4 Summary of the Event Selection . . . 53
- 4.3 General Data Quality after Preselection . . . 53

5 Search for Antiprotons 62
- 5.1 Preselection . . . 62
- 5.2 Selection by $\mathrm{d}E/\mathrm{d}X$ . . . 62

5.3 Albedo Rejection 66
5.4 Mass Measurement by TOF 66
5.5 Antiproton Candidates 66
5.6 Background estimation 69
5.7 Summary of search for Antiprotons 80

6 Determination of the $\bar{p}/p$ Ratio **93**
6.1 Number of Observed Protons and Antiprotons 93
6.2 Correction for Energy Loss 94
6.3 Instrumental Inefficiency 95
6.4 Interaction Loss in the Atmosphere 98
6.5 Secondary Production 98
6.6 Calculation of the $\bar{p}/p$ Ratio 102
6.7 Systematic Errors 104

7 Discussion **108**

8 Conclusions **115**

List of Tables

1.1 Summary of experiments carried out to measure the $\bar{p}/p$ ratio 2

2.1 Main specifications of the BESS detector. 8
2.2 Main specifications of the superconducting solenoidal magnet (MAG). 9
2.3 Summary of the T0 trigger 27
2.4 Summary of T1 trigger 31

3.1 Summary of BESS '93 flight data 38

4.1 Summary of preselection. 54

5.1 Properties of $\bar{p}$ candidates. 76

6.1 Parameters for the $\bar{p}/p$ determination. 102
6.2 Systematic error due to the absolute rigidity error. 105
6.3 Summary of systematic errors. 107

List of Figures

1.1 Current summary of all experiments carried out to measure the $\bar{p}/p$ ratio. 5

2.1 (a) Cross-sectional and (b) perspective view of the BESS detector . . 7
2.2 Cross-sectional view of the superconducting solenoidal magnet. 9
2.3 Schematic view of the JET chamber. 10
2.4 Circuit model of the charge division method used for determining the z-coordinate. 12
2.5 Residual distribution of the JET $r\phi$ hit points. 13
2.6 JET chamber $r\phi$ resolution as a function of (a) the drift distance, and (b) the angle ϕ across the cathode wire plane. 13
2.7 Residual distribution of the JET hit points along z-coordinate for (a) single-charged and (b) multiple-charged particles 14
2.8 Diagram showing a cross-sectional view of IDC and ODC. 14
2.9 Diagram showing a cross-sectional view of the IDC and ODC in $r\phi$ plane. 15
2.10 (a) Equipotential and (b) electric-field strength contours of the IDC. . 16
2.11 Read-out scheme for IDC and ODC signals. 17
2.12 Residual distribution of the IDC $r\phi$ hits. 18
2.13 IDC $r\phi$ resolution as a function of (a) drift distance, and (b) angle ϕ with respect to the axial direction. 18
2.14 Corresponding sets of vernier pads. 19
2.15 Scatter plot of the ε parameter of the inner and outer pad. 20
2.16 Spatial resolution of the z-coordinate measurement in the IDC. 20
2.17 Layout of time of flight hodoscope. 21
2.18 Time of flight counter. 21
2.19 Read-out scheme PMT signals 23
2.20 (a) z-position dependence of the PMT charge measured. (b) Charge distribution at the center of the counter ($z = 0$). 24
2.21 (a) Timing resolution of the PMT vs the z-position. (b) Relation between the timing resolution and square root of N_{pe} at the center. . 25
2.22 Schematic diagram of the data acquisition system 26
2.23 BESS trigger scheme 27
2.24 Basic scheme of the track trigger 28
2.25 Block diagram of TT process. 29
2.26 Track trigger efficiency (a) for an $\bar{p}$ search (b) for an antihelium search. 30

2.27 The block diagram of the data processing system using transputer network. 32

3.1 BESS '93 flight path in altitude, latitude vs longitude 36
3.2 House-keeping data on magnetic field, temperature of TOF and Jet chamber. 36
3.3 Acceleration loads during flight. 37
3.4 BESS data process method. 39
3.5 Simulated BESS detector 40

4.1 Method of the rigidity measurement. 43
4.2 Method of the TOF measurement. 44
4.3 Track quality cut–1. 48
4.3 Track quality cut–2. 49
4.3 Track quality cut–3. 50
4.4 TOF quality cut. 51
4.5 Selection by $R_{A_{TOF}}$. 52
4.6 The estimated error of $1/R_t$ in the $r\phi$ fitting. 53
4.7 $\Delta(1/R_t)$ as a function of the absolute rigidity. 55
4.8 $1/\beta$ vs Rigidity of (a) Unbiased Data Sample and (b) M.C. data sample. 56
4.9 Distribution of $1/\beta$. 57
4.10 Fractional $1/\beta$ resolutions vs *beta*. 58
4.11 $\mathrm{d}E/\mathrm{d}X$ of the Unbiased Sample and M.C. sample 59
4.12 $\mathrm{d}E/\mathrm{d}X$ of the stopped protons. 60

5.1 Proton $\mathrm{d}E/\mathrm{d}X$-Band 63
5.2 $\mathrm{d}E/\mathrm{d}X$ spread around the proton $\mathrm{d}E/\mathrm{d}X$ peak. 64
5.3 β^- vs rigidity for all event samples (a) before $\mathrm{d}E/\mathrm{d}X$ cut and (b) after $\mathrm{d}E/\mathrm{d}X$ cut. 65
5.4 m^2_{TOF} distribution. 67
5.5 Close-up view of β^- vs rigidity for negative-charged samples. 68
5.6 m^2_{TOF} distribution (negative rigidity). 70
5.7 m^2_{TOF} distribution of the $\bar{p}$ candidates. 71
5.8 $\mathrm{d}E/\mathrm{d}X$ of the $\bar{p}$ candidates. 72
5.9 Event display of the $\bar{p}$ candidate. 73
5.10 Track and timing quality parameters for $\bar{p}$ candidates –1. 74
5.10 Track and timing quality parameters for $\bar{p}$ candidates –2. 75
5.11 Relative accuracy of the rigidity measurement. 77
5.12 β^{-1} distributions for negative-charged particles before $\mathrm{d}E/\mathrm{d}X$ cut. . . 78
5.13 Intersection point of albedo particles and the BESS base plane. . . . 79
5.14 β^- vs rigidity for M.C. electron (a) before $\mathrm{d}E/\mathrm{d}X$ cuts and (b) after $\mathrm{d}E/\mathrm{d}X$ cut – Try-1. 81
5.14 β^- vs rigidity for M.C. electron (a) before $\mathrm{d}E/\mathrm{d}X$ cuts and (b) after $\mathrm{d}E/\mathrm{d}X$ cut – Try-2. 82
5.14 β^- vs rigidity for M.C. electron (a) before $\mathrm{d}E/\mathrm{d}X$ cuts and (b) after $\mathrm{d}E/\mathrm{d}X$ cut – Try-3. 83

5.14 β^- vs rigidity for M.C. electron (a) before dE/dX cuts and (b) after dE/dX cut – Try-4. 84
5.14 β^- vs rigidity for M.C. electron (a) before dE/dX cuts and (b) after dE/dX cut – Try-5. 85
5.14 β^- vs rigidity for M.C. electron (a) before dE/dX cuts and (b) after dE/dX cut – Try-1. 86
5.14 β^- vs rigidity for M.C. electron (a) before dE/dX cuts and (b) after dE/dX cut – Try-1. 87
5.14 β^- vs rigidity for M.C. electron (a) before dE/dX cuts and (b) after dE/dX cut – Try-2. 88
5.14 β^- vs rigidity for M.C. electron (a) before dE/dX cuts and (b) after dE/dX cut – Try-3. 89
5.14 β^- vs rigidity for M.C. electron (a) before dE/dX cuts and (b) after dE/dX cut – Try-4. 90
5.14 β^- vs rigidity for M.C. electron (a) before dE/dX cuts and (b) after dE/dX cut – Try-5. 91
5.15 Example of the potential back ground event. 92

6.1 Track-rigidity selection efficiency 94
6.2 (a) Geometrical acceptance of BESS and (b) ε_{single} and $\bar{\varepsilon}_{single}$ 96
6.3 Instrumental Efficiencies for protons 97
6.4 Ratio o efficiencies for anitprotons to those for protons. 99
6.5 Efficiency for the atmospheric absorption of protons and $\bar{p}$'s. 100
6.6 Comparison of the proton flux with the secondary proton flux due to collisions in the air. 101
6.7 Comparison of the measured $\bar{p}$ flux with the expected secondary $\bar{p}$ flux due to collisions in the air. 103
6.8 Comparison of the efficiencies calculated using the M.C simulation with those obtained by the flight data. 105

7.1 Comparison of BESS '93 results with other experimental data and theoretical prediction by two cosmic-ray propagation models. 109
7.2 Comparison of the observed interstellar $\bar{p}$ flux with the other experimental and theoretical values. 110
7.3 Comparison of the BESS '93 results with other theoretical models. . . 113

Chapter 1

Introduction

When considered under the standard leaky box (SLB) model [1, 2], cosmic-ray antiprotons ($\bar{p}$'s) are produced by collisions between cosmic-ray nuclei and ambient interstellar matter. Measurement of the $\bar{p}$ flux is important due to the following reasons:

1. Unlike other cosmic-ray nuclei, $\bar{p}$'s are not produced through spallation; hence their spectrum contains direct information on the propagation history of primary protons, which is essential data for elucidating the mechanism of cosmic-ray propagation.

2. Although $\bar{p}$'s are produced by the following processes:

$$p + p \longrightarrow \bar{p} + p + X$$

or

$$p + p \longrightarrow \bar{n} + n + X$$
$$\searrow\ \bar{p} + e^+ + \nu,$$

$\bar{p}$'s with low energies produced in pp collisions are strongly suppressed due to collision kinematics. This phenomenon is briefly explained as follows. Under the natural assumption that in interstellar space one proton is at rest and the other collides with it, the above reactions can only occur when the incident proton has an energy above 6 GeV in the laboratory frame, which results in the secondary products being carried forward with respect to the direction of the incident proton. As such, low-energy $\bar{p}$'s are only produced when $\bar{p}$'s are emitted backward in the center-of-mass (CM) frame. The suppression of low-energy $\bar{p}$ production is subsequently due to the small probability that $\bar{p}$'s are emitted into the small phase-space fraction.

Detailed calculations show that the resultant $\bar{p}/p$ ratio is well below 10^{-5} at energies less than 1 GeV. Fortunately, because of this low "background" feature, measurement of $\bar{p}$'s with energies below 1 GeV enables restrictions to be placed on the several physical models that produce $\bar{p}$'s at low energies.

Two experimental techniques have been mainly applied to measure $\bar{p}$'s. One method involves the determination of characteristic radiation emitted during $\bar{p}$ annihilation, where measurement sensitivity exists only at low energies where most $\bar{p}$'s are annihilated, though problems arise due to the occurrence of many spurious types of radiation that can mimic $\bar{p}$'s. On the other hand, however, this method has an advantage in that $\bar{p}$'s can be detected down to a very low energy where other methods have no sensitivity. The second method involves identifying $\bar{p}$'s by measuring the momentum of particles in a magnetic field and then determining corresponding velocities, being advantageous in that particle species are clearly identified over a wide energy range event-by-event. This method though, has a drawback in that a strong magnetic field must be generated, which increases the amount of material, thus making it difficult to detect $\bar{p}$'s at very low energies. In addition, the geometrical acceptance is limited by the size of the magnetic field.

Table 1.1: Summary of experiments carried out to measure the $\bar{p}/p$ ratio .

Energy (GeV)	$\bar{p}/p$ ratio	Reference	Technique
< 0.7	$< 3 \times 10^{-3}$	Aizu *et al.* (1961) [3]	annihilation-emulsion
< 0.2	$< 9 \times 10^{-4}$	Apparao (1967) [4]	annihilation-emulsion
$0.2 \sim 2$	$6^{+14}_{-5} \times 10^{-5}$	Bogomolov *et al.* (1987) [6]	permanent magnet
$2 \sim 5$	$2.4^{+2.4}_{-1.3} \times 10^{-4}$	Bogomolov *et al.* (1990) [7]	permanent magnet
$4.7 \sim 11.6$	$(5.2 \pm 1.5) \times 10^{-4}$	Golden *et al.* (1979) [5]	superconducting magnet
$0.13 \sim 0.37$	$(2.2 \pm 0.6) \times 10^{-4}$	Buffington *et al.* (1981) [8]	annihilation-counter
$0.1 \sim 0.64$	$< 2.8 \times 10^{-5}$	Salamon *et al.* (1990) [9]	superconducting magnet
$0.64 \sim 1.58$	$< 6.1 \times 10^{-5}$	Salamon *et al.* (1990) [9]	superconducting magnet
$0.12 \sim 0.64$	$< 4.2 \times 10^{-6}$	Stochaj *et al.* (1990) [10]	superconducting magnet
$0.6 \sim 0.8$	$< 7 \times 10^{-5}$	Moats *et al.* (1990) [11]	superconducting magnet

In 1961, Aizu *et al.* [3] initially reported an upper limit on the $\bar{p}/p$ ratio measured via a nuclear emulsion technique, though since then, balloon-borne experiments have been carried out (Table 1.1). Golden *et al.* [5] later launched a spectrometer containing a superconducting magnet and observed 24 $\bar{p}$'s in the energy range from 5.6 to 12.5 GeV: a result that exceeded the SLB model predictions by 3σ. Bogomolov *et al.* [6, 7] instead used a permanent magnet spectrometer, and also found an excess $\bar{p}$ flux between $0.2 \sim 5$ GeV. The most surprising result, however, came from Buffington *et al.* [8], who detected 28 $\bar{p}$'s using a spark chamber that could identify annihilation radiations, with their measurement of the $\bar{p}/p$ ratio in the energy range from 130 to 320 MeV being two orders of magnitude greater than that predicted by the SLB model.

Such conflicting measurements, especially those on low energies, has led to generating theories that have radically changed the propagation model of $\bar{p}$'s, while also providing a novel mechanism for their production.

The closed galaxy model by Rasmussen and Peters [13] and Peters and Westergaad [14] suggests that protons are totally confined within the galaxy, and consequently, the material through which they pass is an order of magnitude larger than that predicted under the SLB model, which accounts for the presence of excess $\bar{p}$'s. Within the context of the closed galaxy model, Tan and Ng [48] explained both the low- and high-energy (2–12 GeV) data by considering that $\bar{p}$'s undergo a non-annihilating deceleration process. The "thick source" model [16, 17, 18, 19] suggests that $\bar{p}$'s are initially produced in the thick material surrounding a supernova (SN), and are subsequently adiabatically decelerated to a low energy. In fact, Stephens and Mauger [19] showed that if 70% of all SNs are surrounded by dense clouds, then this can explain the low-energy $\bar{p}$ data.

To avoid kinematic suppression of $\bar{p}$'s at low energies, Dermer and Ramaty [20] proposed a model in which target protons are in a high-temperature plasma state such that head-on collisions between the incident and target protons can produce low-energy $\bar{p}$'s. This state may possibly be realized in the accretion disc around black holes or neutron stars, i.e., a strong magnetic field enables only antineutrons to escape confinement and later decay into low-energy $\bar{p}$'s.

Since All these models involve modifying the propagation mechanism for all kinds of cosmic-rays, they affect the propagation and production of $\bar{p}$'s and other types of cosmic matter, e.g., γ-rays, electrons, positrons, light nuclei (Li, Be, B), and heavy nuclei (C, N, O), thereby making makes it difficult to explain all observed data without generating contradictions.

This problem can be avoided, however, if the excess $\bar{p}$ flux is considered to be caused by a novel mechanism. In fact, much speculation has occurred to explain this flux. Among the most intriguing is a model in which $\bar{p}$'s originate from annihilation of weakly interacting massive particles (WIMPs), which might be contained in the Galactic dark matter [21, 32, 23, 24]. The supersymmetric model, which is a natural extension of the standard model, predicts that the lightest supersymmetry particle (LSP) is a WIMP candidate; i.e., although LSP's are stable due to R-parity conservation, they can still be annihilated into quark pairs or gluons which are subsequently fragmented into $\bar{p}$'s and other particles. The most probable respective LSP candidate is a neutralino (the mixed state of a photino, zino, and higgsino, which are super partners of a photon, Z^0, and Higgs particle, respectively). Rudaz and Stecker [36] explained both low- and high-energy data by optimizing the higgsino mass. Recent calculations by Jungman and Kamionkowski [26] suggest that the $\bar{p}$ flux arising from the annihilation of neutralinos into a two-gluon final state is competitive with a tree-level annihilation process. In a certain parameter space, they predict the measurable $\bar{p}$ flux to have a $\bar{p}/p$ ratio $\approx 10^{-5}$, being the level at which the present experiment can reach. It should be noted that the $\bar{p}/p$ ratio predicted by each of these models has a distinctive shape, i.e., almost constant at low energies with a cut-off at the energy corresponding to the mass of a neutralino.

Kiraly and Turner showed that primordial black holes (PBHs) [27], which may have been formed in the early universe, can explain the $\bar{p}$ flux [28]. According to Hawking radiation theory, black holes with mass M emit particles like a blackbody

radiation with temperature expressed by

$$kT = \frac{\hbar c^3}{8\pi GM} \simeq 1.06 \left(\frac{M}{10^{13}\mathrm{g}}\right)^{-1} \mathrm{GeV},$$

and should evaporate in time t_{evap}, where

$$t_{evap} \propto M^3.$$

According to detailed calculations [41], PBHs with a mass of M_* ($\equiv 5.3 \times 10^{14}$ g) are thought to have just started evaporating and emitting detectable $\bar{p}$'s. Under this model, the resultant $\bar{p}/p$ ratio shows a nearly constant value below 1 GeV.

Brown and Stecker [29], Sato [30], and Stecker [31] discussed a model in which, if CP symmetry is spontaneously broken, a global domain may exist that is composed of antimatter, with $\bar{p}$'s from that domain being diffused into our Galaxy. Stecker and Wolfendale [32] suggested that a roughly equal number of $\bar{p}$'s and protons enter our Galaxy from an extra-galactic source and have an energy dependence of $E^{-2.0}$. Since the proton spectrum is known to decrease with energy per $E^{-2.7}$, the resultant $\bar{p}/p$ ratio must then increase with energy per $E^{0.7}$. Such a domain, however, would have to be comprised of two parts separated by the super-cluster, i.e., 100 Mpc, otherwise it is inconsistent with the null γ-ray annihilation signal arriving from the boundary region between super-clusters.

Recent measurements searching for low-energy $\bar{p}$'s at a level approaching a $\bar{p}/p$ ratio $\approx 10^{-5}$ have set stringent upper limits on the $\bar{p}/p$ ratio , being in contradiction with the result of Buffington *et al.* , and strongly suggesting the suppression of $\bar{p}$ production at low energies. To investigate the above-mentioned model of the cosmic-ray propagation or possible new mechanisms of $\bar{p}$ production, higher sensitivity measurements are required. Figure 1.1 summarizes known $\bar{p}/p$ ratio measurements and also the fluxes predicted by various models.

To search for $\bar{p}$'s down to a $\bar{p}/p$ ratio of $\approx 10^{-6}$, a new balloon-borne experiment, named "a Balloon-borne Experiment with a Superconducting magnet rigidity Spectrometer (BESS)", is designed based on several new concepts; (1) precise measurement of momentum by a magnetic spectrometer using a thin superconducting solenoid and (2) use of large tracking detectors having a large geometrical acceptance. After construction and detailed performance checks of these detectors, cosmic-rays were first measured in the summer '93. In this dissertation, I will describes experiment results of our state-of-the-art search for low-energy $\bar{p}$'s.

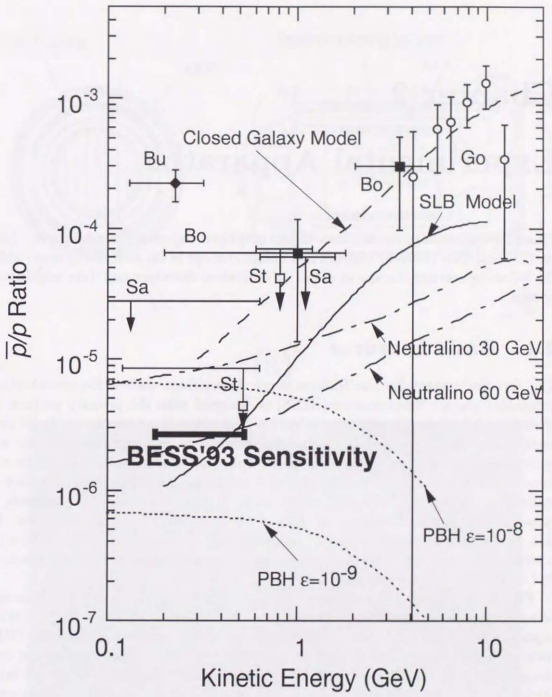

Figure 1.1: Current summary of all experiments carried out to measure the $\bar{p}/p$ ratio. The open circles are from Golden *et al.* [5], the black squares from Bogolomov *et al.* [6, 7], and the black diamond from Buffington *et al.* [8]. The open squares are upper limits from the LEAP experiment [10, 11], while the upper limit at the lowest energy is from Salamon *et al.* [9]. The solid and dashed lines respectively represent the SLB and closed galaxy models. Also shown are two curves for the neutralino model and two curves for the PBH model using with different parameters. These spectra have been modified to take solar activity into account. The sensitivity of BESS '93 is shown as a bold line.

Chapter 2

Experimental Apparatus

This chapter provides an overview of the employed experimental apparatus. Section 2.1 describes the basic features and design concept of the detector system, while the following sections discuss in detail its individual detectors and data acquisition system.

2.1 Basic Features

The detector system for the Balloon-borne Experiment with a Superconducting Solenoidal magnet Spectrometer (BESS) is designed with the primary purpose to investigate high energy cosmic particles, i.e. , cosmic antimatter, especially $\bar{p}$'s and antiheliums. BESS has a large geometrical acceptance and high capability for executing precise event recognition suitable for distinct detection of rare cosmic antimatter existing among an abundance of protons and heliums. Such efficiency is realized by combining three key technologies: a thin superconducting magnet, a cylindrical-configured tracking detector, and a rapid data acquisition system. In fact, these features also enable searching for other kinds of rare cosmic rays, e.g., positrons, gamma-rays, and isotopes, as well as precisely measuring the absolute flux of primary protons and heliums.

Figure 2.1 shows a cross-sectional view and photograph of the BESS detector, being comprised of a jet-type drift (JET) chamber, inner drift chambers (IDCs), superconducting solenoid, outer drift chambers (ODCs), and a time of flight (TOF) counter. These components are arranged radially from the center of the device, and along with the front-end electronics and microcomputers, are enclosed by a 2-mm-thick aluminum pressure vessel that is pressurized during flight. Situated outside the vessel are an 8-mm tape storage device shielded by iron containers, a power supply system, and a consolidated instrument package (CIP) communication unit which handles communications between the payload and ground station. The entire unit weighs 2.1 t and is 1.5 m in diameter and 3.2 m in length. When suspended from a 2.7-Mft^3 balloon, it is compact and light enough to travel at an altitude of about 35 km.

A thin entrance wall of about 7.5 g/cm^2 enables low energy particles to pass through the detectors, while a cylindrical configuration provides large tracking vol-

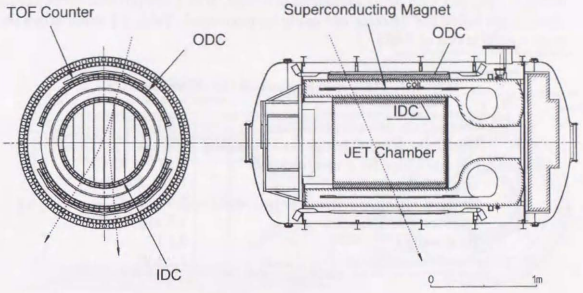

(a)

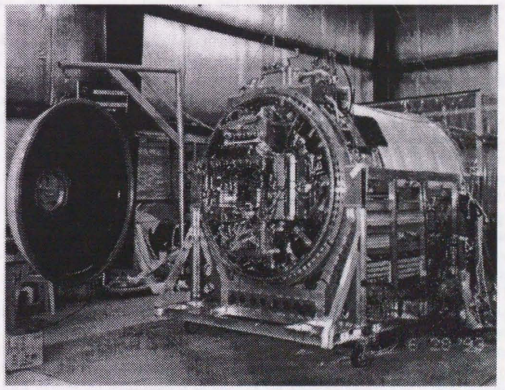

(b)

Figure 2.1: (a) Cross-sectional view and (b) photograph of the BESS detector

ume and a geometrical acceptance of ~ 0.5 m^2 sr. The JET chamber is capable of precisely detecting particles and measuring their rigidities. Since the tracking device is equipped with 32 measurement positions, even a complicated event having interactions inside the detector can easily be monitored. Table 2.1 summarizes the main specifications of BESS.

Table 2.1: Main specifications of the BESS detector.

Geometrical acceptance	0.4 m^2 sr
Maximum detectable rigidity in tracking	200 GV
Rigidity range for $\bar{p}$ identification	0.45 – 1.05 GV
Trigger rate	100 – 200 Hz
Material in the spectrometer (per wall)	7.5 g/cm^2
Pressure vessel dimension	1.5 m$\phi \times$ 3.2m
Total weight	2.1 t
Power consumption	1.2 kW

2.2 Superconducting Solenoidal Magnet

Figure 2.2 shows cross-sectional views of the superconducting solenoidal magnet (MAG), which has a 0.8 m$\phi \times$ 1.0 m warm bore that encloses the JET and inner drift chambers. A magnetic field of 1 T (maximum 1.2 T) is generated inside the bore at a nominal current of 520 (540) A, with the resultant field uniformity being $\pm$15%. A solenoid coil (1 m$\phi \times$ 1 m (ℓ) $\times$ 5.4 mm (t)) made of aluminum-stabilized superconductor NbTi(Cu) is installed inside the double thermal shielded cryostat, and is indirectly cooled through the aluminum cylinder by a toroidal-shaped liquid helium reservoir tank with 150-ℓ capacity (static indirect cooling method) [37]. This method has an advantage over the bath cooling method in that it allows using a thinner cryostat wall. The MAG's thickness including the cryostat is 0.21 radiation length per wall and its total weight with helium is 430 kg. The amount of stored energy at 1 T is 815 kJ. Pure aluminum strips (PAS [37]) are attached to the inner surface of the solenoid for quenching, i.e. , they rapidly conduct thermal energy in the axial direction and homogenize the thermal distribution. Table 2.2 summarizes the main specifications of the MAG.

The magnet is equipped with a persistent current switch (PCS) fabricated from a superconductor and heater. It is heated up to break the superconduction during magnet excitation, then cooled and automatically shortcut after being charged. The current from the magnet is subsequently able to pass through the PCS. Since the decay constant of this current is more than 900 years, if helium is filled to its maximum level, the current persists for as long as 6 days with no energy supply to the magnet. The magnet can be safely discharged by switching off the PCS and shunting the magnet current into a resistor located external to the vessel.

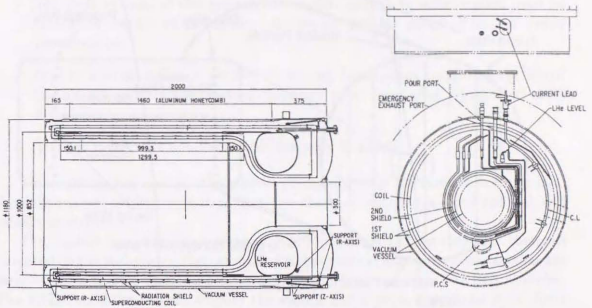

Figure 2.2: Cross-sectional view of the superconducting solenoidal magnet.

Table 2.2: Main specifications of the superconducting solenoidal magnet (MAG).

Dimensions	
Coil diameter	1.0 m
length	1.3 m
coil thickness (center)	5.2 mm
(end notch)	10.4 mm
Cryostat diameter	1.18 m
length	2.0 m
Useful aperture diameter	0.85 m
length	1.0 m
Central field	1.0 T
Current	500 A
Maximum field	1.2 T
Stored energy	815 kJ
Wall thickness	0.21 X_0
Total weight	430 kg
Conductor	Nb/Ti/Cu
Stabilizer	Pure Al(99.999%)

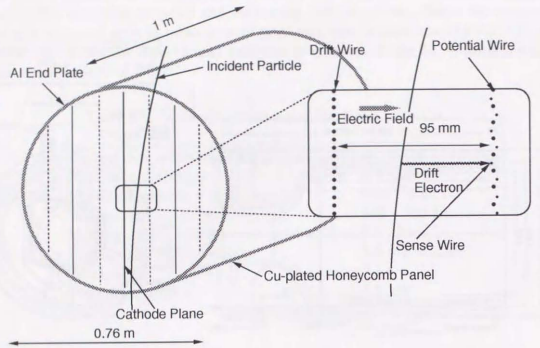

Figure 2.3: Schematic view of the JET chamber.

2.3 JET chamber

The JET chamber is a cylindrical drift chamber situated inside the magnet, (Fig. 2.3) having a tracking volume of 0.754 mϕ × 1 m.

Cathode planes partition the chamber into four sections, with each plane consisting of 100 aluminum wires with a 250-μm diameter. The wires are laid out, though actually they are stretched, at 6.75-mm intervals, and a high voltage of 10.8 kV is applied to produce a constant electric field which drifts ionized electrons to the sense wires. At the center of each section, the sense and potential wires are alternately laid out at 13.4-mm intervals. The sense and potential (cathode) wires are respectively 20-μmϕ gold plated tungsten-rhenium wires and 200-μmϕ gold-plated aluminum wires, and are stretched with a tension of 55 and 400 gw. To minimize wire loosening due to creep, before being soldered, the wires were pre-stretched with a tension of 15 and 40 gw, respectively. The sense wires are staggered by 0.5 mm to resolve left-right ambiguity. The outer two sections have 32 sense wires and 33 potential wires, while the inner two correspondingly have 52 and 53 wires. The maximum drift distance of ionized electrons is 95 mm.

The cylindrical side walls are made of alamyd core honeycomb to minimize material thickness and weight. The inner surface of the honeycomb panel is made of a copper-plated KAPTON sheet, on which the field-shaping patterns are etched. The two end-plates are 25-mm-thick aluminum discs. The chamber's total weight is 60 kg.

The chamber is filled with a mixture of 90% CO_2 and 10% Ar, being suitable for

this experiment due to the following reasons:

1. The drift velocity of this gas mixture is slow enough to achieve good position resolution using a relatively slow electronics package designed for low power consumption.

2. Due to a small diffusion coefficient, timing fluctuations caused by the longitudinal diffusion of the electron cloud are small even after a long drift of 95 mm.

3. The gas mixture is non-flammable and easy to handle.

This mixture was used for the other drift chambers for the same reasons, in fact, the entire vessel is filled with it so that any chamber suffering a small gas leak will remain operational.

The signals from the sense wires are picked up by 112 preamplifier channels mounted on the end-plates, then amplified and converted into voltage signals that are directly fed into 28.5-MHz flash-type analog-to-digital converter (FADC) modules. The FADC modules further amplify the signals and digitize them into 8-bit digits every 35 ns. Since each FADC output contains information on the charge, timing, and shape of each pulse, multiple hits in a single wire can be well separated and recognized. However, the total amount of FADC data is too large to record all, and consequently, on-line zero-suppression circuits and a data compression scheme are employed to reduce the data amount by a factor of 3 at the expense of a slight loss of information. Briefly, digitized data is discriminated by a digital comparator and only data above a threshold value is accumulated into first-in-first-out (FIFO) memory. Data compressors then sequentially read these data and successively compress it into a cluster. Each compressed cluster contains principal information on the total integrated charge, timing, first two raw pulse height data, and width. The entire process takes 100 μs.

The position of the hits are three-dimensionally measured by the timing and charge of the signals. In this dissertation, cylindrical coordinates ($r\phi z$) are used, with the magnet field direction being defined as the z-axis and the perpendicular plane as the $r\phi$ plane. The hit position in the $r\phi$ plane is calculated by its drift time. Although drift length x and drift time t are nearly proportional, some nonlinear effects nevertheless exist due to distortion of the electric field and inclination of the track in the cell. Such nonlinearity, however, is corrected by fitting the deviation of the hit position to a third-ordered polynomial. The hit position along the z-coordinate is obtained by applying the charge division method, where Fig. 2.4 shows the employed circuit model. To minimize errors, the internal resistor and gain of the preamplifier are calibrated and adjusted using the actual flight data.

The FADCs read signals from 80 sense wires, of which 32 are read from both ends to determine the z-coordinate via charge division method. As the tracks pass through the central two layers of wires, a maximum of 24 and 16 positions can be measured in the $r\phi$ plain and z direction, respectively. Based on the residuals obtained from the fitted track (Fig. 2.5), the overall resolution of $r\phi$ plane is estimated

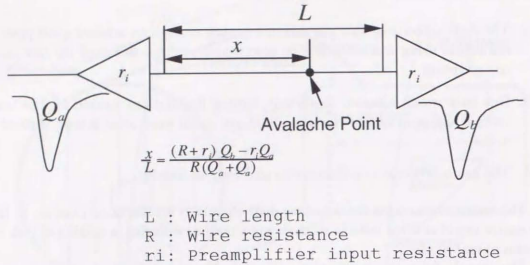

Figure 2.4: Circuit model of the charge division method used for determining the z-coordinate.

to be 200 μm. These resolutions are dependent on the drift length due to the diffusion of electrons. Figure 2.6 shows the resolution as a function of the drift distance (a) and the angle of the track trajectory across the cathode wire plane (b), where both resolutions are gradually degraded according to the drift distance and angle.

The resolution of the z-coordinate measurement is 2.5 cm for single-charged particles (Fig. 2.7 (a)), being worse than the expected value of 1 cm, since all the charge information below the threshold value is lost using the zero-suppress and compress scheme, and cannot be precisely corrected. On the other hand, 1.5-cm resolution is obtained for multiple-charged (Fig. 2.7 (b)) because they reduce the threshold effect.

2.4 Inner and Outer Drift Chamber

The inner drift chamber (IDC) and the outer drift chamber (ODC) are cell-type arc-shaped drift chambers located inside and outside the magnet, respectively (Fig. 2.8). The IDC (ODC) is a 1.06-m-long (1.18 m) and 36-mm-thick (44 mm) chamber located between the radii of 384 mm (594 mm) and 420 mm (638 mm) covering a polar angle from 8 (18) to 172 (162) degrees. Both chambers are identical except for their dimensions and magnetic field strength, i.e. , 1 T for the IDC and about 0.1 T for the ODC. The mechanical structure of each chamber is composed of four alamyd core honeycomb panels with end and side plates made of engineering plastic (G10). Figure 2.9 depicts a cross-sectional view of the $r\phi$ plane, where the surface of the panel is made of 18- and 125-μm-thick copper and KAPTON sheets, respectively. The outer surface of the Cu sheet is covered with a 0.5-mm-thick Al sheet to increase mechanical strength. The inner KAPTON sheet is etched at 3-mm interval to form

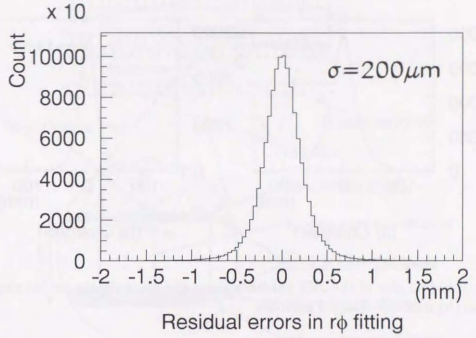

Figure 2.5: Residual distribution of the JET $r\phi$ hit points.

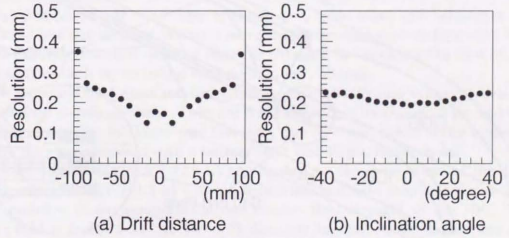

Figure 2.6: JET chamber $r\phi$ resolution as a function of (a) the drift distance, and (b) the angle ϕ across the cathode wire plane.

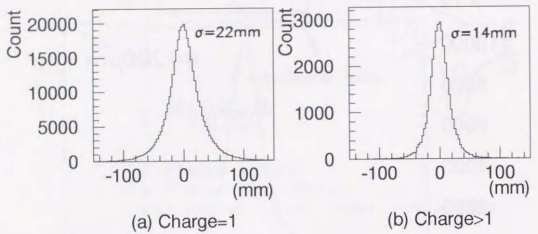

Figure 2.7: Residual plot of the JET chamber along the z-coordinate for (a) single-charged and (b) multiple-charged particles

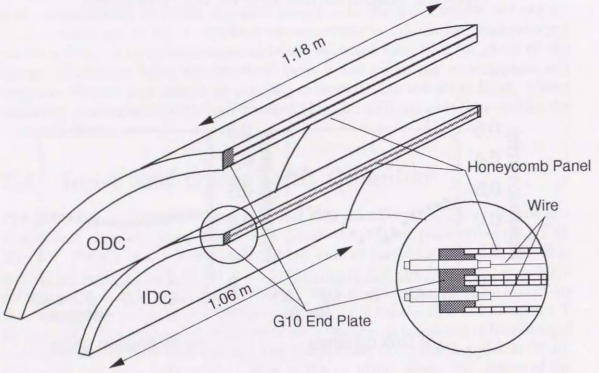

Figure 2.8: Diagram showing a cross-sectional view of IDC and ODC.

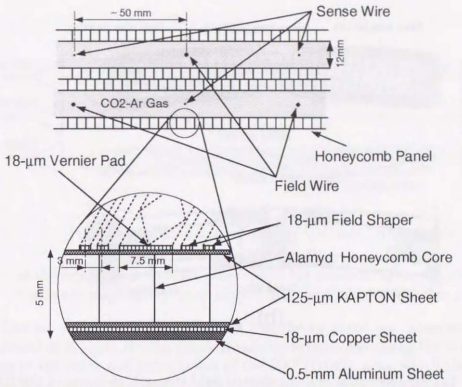

Figure 2.9: Diagram showing a cross-sectional view of the IDC and ODC in $r\phi$ plane.

a 1.5-mm-wide and 18-μm thick electric field shaper, and corresponding pairs of 7.5-mm-wide and 18-μm-thick diamond-shaped vernier pads surround the sense wires to detect the z-coordinate position. The inside of the chamber is divided into two 12-mm-thick layers. At the center of each layer, sense wires and field wires are alternately laid out in about 50-mm spacing intervals. This wire configuration also acts to calibrate the drift velocity which is obtained by adjusting the sum of the drift length of both layers to the wire spacing, i.e. , 50 mm.

The sense and field wires are respectively gold-plated 25-$\mu m\phi$ tungsten-rhenium and 250-$\mu m\phi$ aluminum wires. They are stretched with a tension of 55 gw and 400 gw, respectively. To minimize wire loosening due to creep, before being soldered, the wire were pre-stretched with a tension of 15 and 40 gw, respectively.

A high voltage of 2.7 kV (2.6 kV) is applied to the sense wires of the IDC (ODC), while –4.0 kV (–4.5 kV) to the field wires and field shapers. Figure 2.10 shows contours of the equipotential and electric field strength of the IDC. The electric field is inclined 5.5° to the drift direction to compensate for the Lorentz angle produced by the magnetic field, and is constant across most of its drift region. The shape of the ODC's electric field is almost the same as the IDC's, with the exception that the Lorentz angle is negligibly small.

Both chambers are filled with the same gas mixture used in the JET chamber (90% CO_2, 10% Ar).

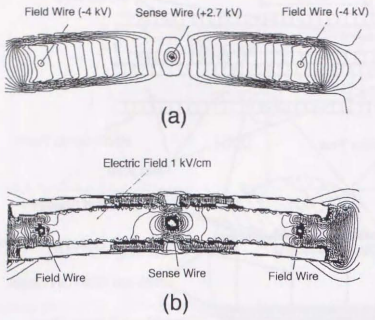

Figure 2.10: (a) Equipotential and (b) electric field strength contours of the IDC.

The chamber signals from the sense wires and vernier pads are both amplified by preamplifiers mounted on an aluminum plate attached to the end-plate. Figure 2.11 shows a diagram depicting the read-out scheme of the IDC and ODC, where one signal is read from each IDC sense wire, two for each ODC sense wire, and four signals are read from each corresponding pair of vernier pads. Thus, a total of five or six signals are obtained per IDC or ODC sense wire. As explained next, these signals are distributed among amplifier and discriminator (AMP/DISCRI) modules, analog-to-digital converter (ADC) and time-to-digital converter (TDC) modules, and flash-type analog-to-digital converter (FADC) modules.

1. The IDC and ODC sense wire signals are amplified and discriminated in the AMP/DISCRI modules. If the discriminated signal in the inner and outer layer of each chamber coincide, they are fed through the track trigger (TT) module, which performs a rapid analysis of their rigidity (see Section 2.6.1).

2. The ODC sense wire signals are then fed to the TDC modules which convert their timing into 12-bit digits, while the ODC vernier signals are processed by the ADC modules which integrate their charge during a 500-ns gate and convert them into 12-bit digits. The timing information is utilized for determining the hit position of the ODC in the $r\phi$ plane, while the charge information for determining the hit position along the z-axis.

3. The IDC vernier signals are processed and converted into timing and charge information by 28.5-MHz FADC modules and compressors in the same manner

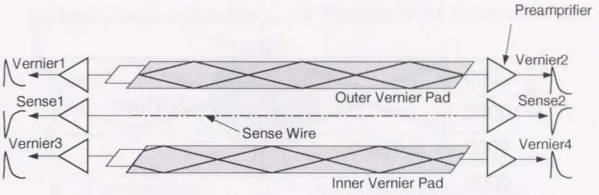

Figure 2.11: Read-out scheme for IDC and ODC signals.

as the signals from the JET sense wires. Hit positions in the $r\phi$ plane and along z-axis are respectively determined using the timing and charge information.

The hit positions of the IDC (ODC) in the $r\phi$ plane are determined using the measured drift time. Briefly, the drift velocity is calibrated using the sum of the drift times of the inner and outer layers of the IDC (ODC), after which the polynomial corrections are applied to minimize errors in the tracks. The overall resolution of the $r\phi$ plane is estimated to be 200 μm based on the residuals obtained from the fitted track (Fig. 2.12). Figure 2.13 shows the IDC's $r\phi$ resolution as a function of the drift distance (a) and the angle of the track trajectory with respect to the axial direction (b), where both resolutions are gradually degraded according to the drift distance and angle.

The hit position along z-axis is measured using the signals generated on the corresponding sets of vernier pads, i.e. , each pad is situated on the inner and outer KAPTON sheet such that they surround one sense wire. Each set is cut as shown in Fig. 2.14, having a cycle of 100 mm for the IDC (120 mm the ODC). The corresponding set of pads are situated such that they are shifted along z-direction by a quarter cycle with respect to another.

When the drifted electrons avalanche near a sense wire and deposit their charge on it, induced signals are generated on the corresponding set of pads. The charge on each pad is divided into the two parts (A and B) of the pad and the both charge are separately read out. We define the normalized charge ratio of A and B for each pad as:

$$\varepsilon_{I(O)} = \frac{Q_{AI(O)} - Q_{BI(O)}}{Q_{AI(O)} + Q_{BI(O)}}$$

where $Q_{AI(O)}$, $Q_{BI(O)}$ are the charge on A and B for inner pad (outer pad). Each ε parameter is linearly related to the z-axis position of the avalanche point. Figure 2.15 shows the scatter plot of the ε parameter. One cycle around the round square locus represents a movement of 100 mm (120 mm) along z-axis. The line in the figure shows the ε_I and ε_O calculated numerically for various z-position. We can then derive the hit position along the z-coordinate by comparing the measured ε pair to

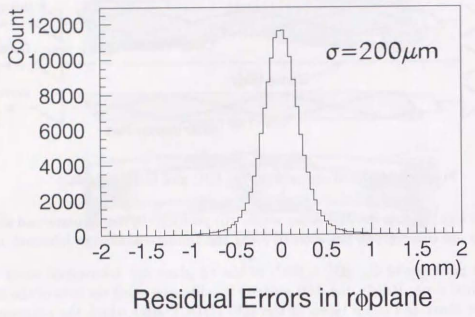

Figure 2.12: Residual distribution of the IDC $r\phi$ hits.

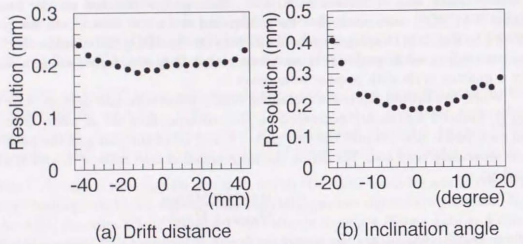

Figure 2.13: IDC $r\phi$ resolution as a function of (a) drift distance, and (b) angle ϕ with respect to the axial direction.

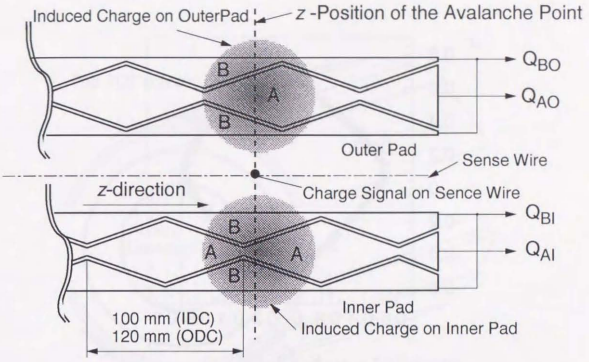

Figure 2.14: Corresponding sets of vernier pads.

the numerical calculation. The spread of the measured ε values around the numerical line provide the estimation of the z-axis resolution (Fig 2.16). When the coarse z-position obtained by the charge division of the JET chamber, absolute z-position can be determined by the precision of 350 μm.

2.5 Time of Flight Hodoscope

The Time of Flight hodoscope (TOF) consists four upper and six lower plastic scintillation counters with a dimension of 110 cm × 20 cm × 2 cm. They are placed just outside the ODC at the radius of 65 cm (Fig. 2.17).

The light signals of the scintillation paddle are guided adiabatically through the acryl light guide to the photo-multiplier tubes (PMTs) at both ends. For a daily check and calibration use, there equipped a light-emitting-diode (LED) at the center of the scintillator, and the connector for the laser light are fitted to the side wall of the light guide. The whole counter is wrapped with one layer of aluminized mylar and four layers of black vinyl sheet to reflect the light and to shield the light from outside, respectively. Figure 2.18 shows the schematic view of the single TOF counter.

Since the PMTs are operated in the magnetic field of 1.8 kG, where ordinary PMTs could not be used, we use PMTs with 19 stages of mesh-typed dynodes, H2611SX (Hamamatsu photonics), which is specially designed for usage in a high

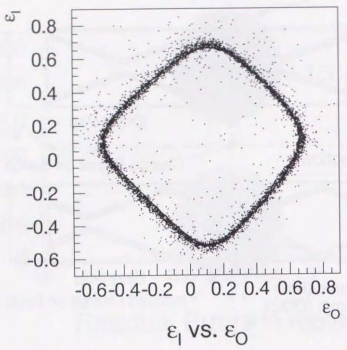

Figure 2.15: Scatter plot of the ε parameter of the inner and outer pad.

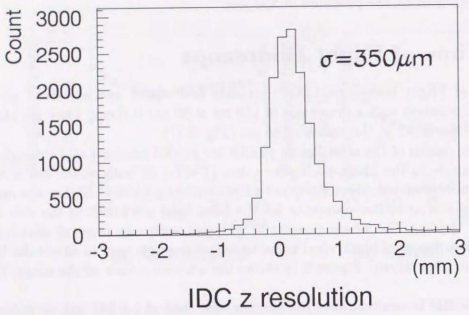

Figure 2.16: Spatial resolution of the z-coordinate measurement in the IDC.

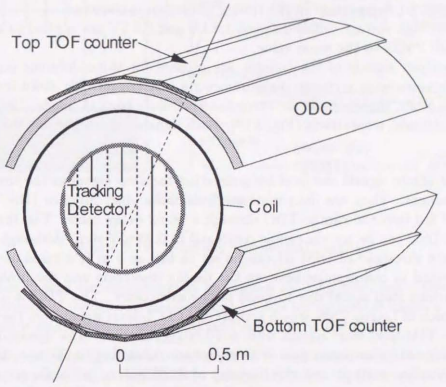

Figure 2.17: Layout of time of flight hodoscope.

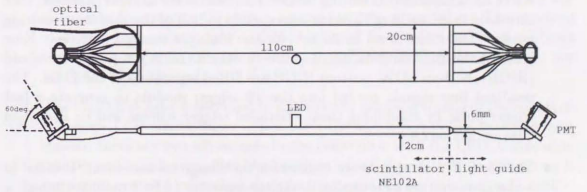

Figure 2.18: Time of flight counter.

magnetic field. Besides, to reduce the effect of the field, the axis of the PMT is aligned with the field direction by 15 degrees. The test of PMT in the 1.8 kG reveals that the PMT gain increases by at most 10% and the timing shifts by 100 ps, however, no degradation in the timing resolution is observed.

Various high voltage values between 1.8 kV and 2.3 kV are applied to adjust the gains of all PMTs to the same value.

The output signals of the counter are utilized for three different purposes; a timing measurement, a charge measurement, a fast trigger. To avoid interference with each other, three signals are extracted separately from th anode, 19th dynode, and 18th dynode, respectively (Fig. 2.19). Each signals are processed in the following ways:

- The anode signals are used for generating the stop signal in the timing measurement. They are discriminated by a camac discriminator (DSC) module and fed into the camac TDC through a 50-ns delay cable. The threshold of the DSC can be set via camac command in 0.23 mV step. Although the minimum threshold of DISCRI can be set as low as 5 mV, a value of 10 mV is selected to compromise between the timing resolution and the probability of spurious stop signal due to noise of the electronics. The TDC is a modified version of Lecroy 2208, which accepts eight ECL-level signal from the DSC and one NIM-level start signals from a T0 trigger module. The dynamic range is 11-bits and conversion gain is 50 ps/count. According to the test, the timing resolution of 70 ps and the linearity of 0.1% over a full scale are obtained. Since inductive parts are used in the oscillator circuit, the timing conversion gain is shifted by 2.5% in the actual operating field. However there is no effect on TDC resolution and linearity.

- The 19-th dynode signals are used for generating a fast trigger signal. First each PMT signal at the both ends is summed up after integration with time constant of 20 ns to reduce the position dependence of the signal amplitude. The summed signals are fed into the two-level discriminator (2LD) modules, which has a capability of setting two level thresholds for all eight channels. One threshold is set to 15 mV, which corresponds to half of the minimum ionizing pulses. The other is set to 50 mV for the multiple charged particles. Four kinds of the DSC outputs, i.e., top low-threshold (LOW), top high-threshold (HIGH), bottom LOW, bottom HIGH are ORed separately in the 2LDs. The resultant four signals are fed into the T0 trigger module to generate a fast trigger pulse by combining them. Detailed trigger scheme will be described later in Section2.6.1.

- The 18-th dynode signals are utilized for the charge measurement. It is fed to a charge-to-voltage type analog-to-digital-converter (ADC) module through a 200 ns analog delay line. The charge is integrated during the gate width of 50 ns and converted into 12-bit digits. The conversion gain is 0.6 pC/count. The integrated nonlinearity is below 1 count over the full-scale, which provide a wide dynamic range of charge measurement, from 1/20 to 100 times as large as the charge corresponding to mimimum ionizing particles. The intrinsic resolution of the charge measurement is 10% for minimum ionizing particles, which is dominated by photo-electron statistics in the PMT.

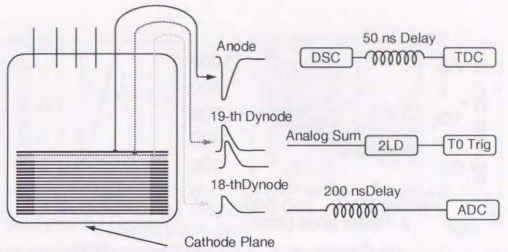

Figure 2.19: Read-out scheme PMT signals

The gain and timing of each counter were first calibrated using the beams from the proton synchrotron at KEK before the installation. Protons and pions with 1 GeV/c is used to determine the high-voltage applied to each counter and parameters for a time-walk correction.

After installation into the BESS detector, the gain and the timing are monitored and calibrated both in the ground and in the flight situation by the following three ways:

1. The laser light pulser (Hamamatsu PLP-02) is used for the precise measurement of the TDC conversion gain and timing offset for each counter in the actual operating condition. The output light has a wave length of 410 nm and is led into the counter through a 1-mm-diameter quartz fiber. The excellent stability of the pulse height and the timing of laser pulse enable to calibrate the timing and gain of each counter, though this calibration scheme is not available when the endcap is closed.

2. The blue LED light is also used to monitor the gain and timing of the counters. Although LED signals have slower rise-time and less stability than the laser signals, there are two advantages in the calibration with the LED. Calibration can be performed even after the pressure vessel closed. PMTs at both ends are simultaneously calibrated and the their gain can be relatively adjusted.

3. In the flight situation, cosmic-rays are used to determine all calibration parameters used in the offline analysis. Since both the gain and the timing fluctuate according to the temperature during the flight, we divided the flight data into several runs and calibrate them in the individual run.

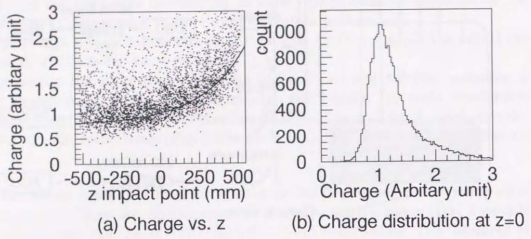

Figure 2.20: (a) z-position dependence of the PMT charge measured. (b) Charge distribution at the center of the counter ($z = 0$).

The performance of the TOF counter is studied using the flight data samples. Figure 2.20 shows the z-dependence of the PMT charge measured for the proton samples with above 3 GeV/c. The line in the figure indicates the fitted curve for the peak of the distribution using the following equation, i.e., $a + be^{cz}$, where a,b, and c are parameters to be fitted. Figure 2.20-(a) shows the charge distribution versus the z position. The resolution determined from the distribution below peak is about 10% at the center of the counter, which means that about forty photo-electrons are obtained for energetic protons. At the center of the counter, the timing resolution of 300 ps is observed. Figure 2.21-(b) shows the timing resolution versus square root of the number of the photo-electrons (N_{pe}). The linear correlation between two variables is clearly observed.

2.6 Data Acquisition System

The BESS data acquisition system (DAQ) is designed for this balloon-borne experiment.

Because of a large geometrical acceptance, a primary trigger rate of the BESS detector exceeds a few thousand per second. This is far above the maximum storage rate of about 200 Hz. The BESS DAQ needs to process these large amount of data and to reduce both the number of events and the data size. The hard-wired data compression scheme reduces event data size by a factor 1/3 and fast hard-wired trigger logic eliminates most of unwanted backgrounds. In addition, multi-processor system gather and packs the event data into an average size of 1 kbyte in 1 ms. Thus the data are reduced to the acceptable rate of 80–90 Hz.

On the other hand, it is also important for the balloon-borne experiment to

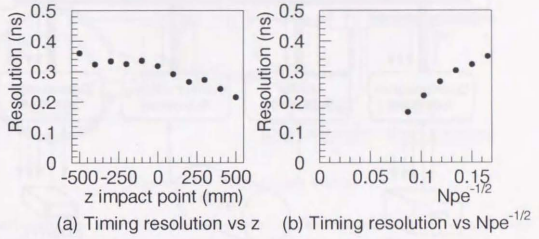

Figure 2.21: (a) Timing resolution of the PMT vs the z-position. (b) Relation between the timing resolution and square root of N_{pe} at the center.

reduce the power consumption. A larger power consumption demands additional batteries and results in a larger total weight or in a shortening flight time. Besides, the heat generated by the electronics is accumulated in the payload and might damage the detectors and electronics. To avoid these problems, most of the electronics are custom-made to minimize the power consumption while keeping the processing speed fast.

Figure 2.22 shows general scheme of the BESS DAQ. Four subsystems functions for following four porposes; event-process, data-storage, monitoring, and communication[39]. Each subsystem is controlled by a microprocessor(NEC-V40 or V50) and is linked with each other through serial bus-lines (Omninet).

Event-process subsystem gathers and processes the event data from each detector when the trigger signal initiates the data acquisition. The processed data are sent to the data-storage subsystem and recorded in two 8-mm EXABYTE tapes. The house keeping data such as temperature or pressure are handled by the monitor subsystem and are transferred to the data-storage subsystem to be recorded in the tapes. The communication subsystem manages communication between the ground station and the payload. Some of the recorded data are telemetered to the ground over a radio link to monitor the detector status during the flight. The commands to control the detector are transmitted to the payload by the communication subsystem.

In following sections, each component of the DAQ is explained in detail.

2.6.1 Trigger

BESS trigger system is designed with a primary objective to detect efficiently $\bar{p}$ and antihelium signals while rejecting most of proton and helium backgrounds. It

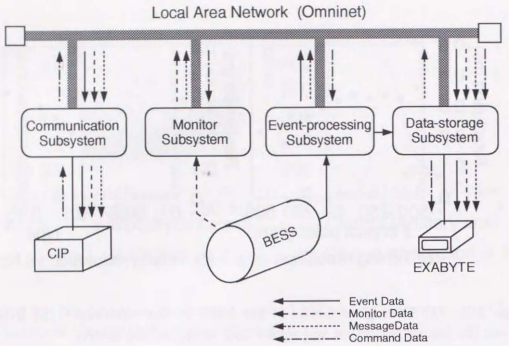

Figure 2.22: Schematic diagram of the data acquisition system

also accepts some portion of other cosmic-ray species such as gamma rays, electrons, positrons, deuterons, tritons, and other heavy isotopes as well as protons and heliums.

Trigger consists of two levels (Fig. 2.23). The first level is a fast "T0 trigger" where the combined signal of the top and the bottom scintillators initiates data acquisition cycle. The second level is a "T1 Trigger" where event reduction is performed through a "track trigger" (TT) or "count down" (CD) logic. The TT scheme selects preferably negative-charged particles judging from the chamber hit pattern, while the CD logic reduces the event rate irrespective of the event configuration. If the event is judged to be accepted by either the TT or CD logic, the T1 trigger approves further data processing. Otherwise the data acquisition cycle is discontinued and all electronics are cleared for the next cycle.

T0 Trigger

The T0 trigger process is done by the T0 trigger module which is controlled by CAMAC commands. The T0 trigger signal comprises four modes for the different physics targets. The first mode is a "T0 Low" aimed for single-charged particles. This mode requires both top and bottom scintillators signal above the low threshold of the 2LD. The second one is a "T0 High" for multiple charged particles. This mode requires both the top and bottom scintillators above the high threshold. The third one is a "T0 gamma" for gamma rays. Gamma-rays can be detected when they are converted to e^+e^- pair at the upper part of the MAG. To accept the events

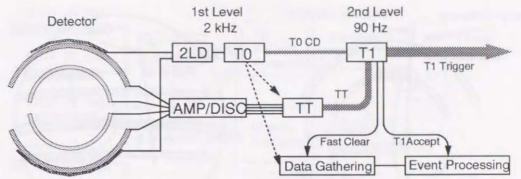

Figure 2.23: BESS trigger scheme

with such a configuration, this mode requires that there is null hit in top scintillators and at least one hit in bottom scintillators. The last one is a "T0 external" which is generated synchronously by the external pulse. This is only used for the calibration.

Logical-OR signal of those four modes initiates data gathering and the track trigger process. The T0 trigger module then locks out the further trigger process until the data acquisition cycle is completed.

The T0 trigger module is equipped with the CD logic for all modes to reduce the trigger rate unconditionally. If the count down number N_{cd} is set for a certain mode, trigger output comes once every N_{cd}. In the '93 flight, a countdown number of 256 was selected for the "T0 gamma" mode to reduce the event rate from 20 kHz to 80 Hz. For "T0 Low" and "To High", the count down number is unity to accept all events at this level.

Table 2.3 summarizes the T0 triggers.

Table 2.3: Summary of the T0 trigger

Mode	Top Low	Top High	Bottom Low	Bottom High	Ext	Count Down	Single Rate	T0 Out
T0 Low	1	*	1	*	*	1/1	2.3 kHz	2.3 KHz
T0 High	*	1	*	1	*	1/1	610 Hz	610 Hz
T0 gamma	0	0	1	*	*	1/256	19 kHz	70 Hz
T0 extern	*	*	*	*	1	0	0	0

1 : Signal should be asserted.
0 : Signal should be negated.
* : Signal is not concerned.

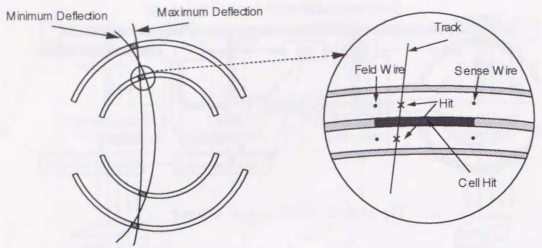

Figure 2.24: Basic scheme the track trigger

Track Trigger

Fig 2.24 shows the basic concept of the TT. First the sense wire signals of each layer are discriminated and fed into the coincidence (COIN) modules. They are then combined into "cell-hit" signals by requiring the coincidence in both layers to eliminate spurious hits caused by electronics noise or local radio-active sources. Total of 30 and 22 cell-hit signals are generated for each ODC and IDC, respectively. Each cell-hit gives coarse position information by the precision of the cell size, i.e. , about 50mm. A Combination of three or four cell-hit positions provides rough estimation of the rigidity of the track. The two tracks in Fig. 2.24 illustrate the maximum and the minimum possible deflection ($\equiv$rigidity^{-1}) for a certain combination of cell-hits. We define the mean value of two deflections as a deflection of the cell-hit combination. By calculating the deflection for all cell-hit combinations and storing them in the look-up table beforehand, a quick rigidity analysis is possible without any time-consuming calculation.

A Track Trigger (TT) module carries out these task using a 2-Mbyte read-only memory (ROM) and a microcode-programmable sequencer (Fig. 2.25). The TT module selects events in two stage; hit-pattern selection and rigidity selection as follows:

- hit-pattern selection

  To eliminate the cell combination which have no possible track or too many hits to scan, event selections based on the cell-hit pattern are applied.

  They are divided into following eight categories depending on the number of cell-hits in the upper ODC (ODC1), upper IDC (IDC1), lower IDC (IDC2), and lower ODC (ODC2):

  1. $\bar{p}$ clean : only one hit in each chamber (1111).

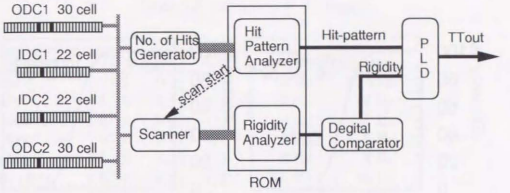

Figure 2.25: Block diagram of TT process.

  2. $\bar{p}$ dirty : two hits in one chamber, and only one in others (1112_p).
  3. $\overline{\text{He}}$ clean : only one hit in each chamber (1111).
  4. $\overline{\text{He}}$ dirty : two hits in one chamber, and only one in others (1112_p).
  5. Missing : no hit in one chamber and one in others (0111_p).
  6. Multi clean : multi-hits in the IDC2 and ODC2 (1113,1123,1124)
  7. Multi dirty : two hits in ODC1 and multi-hit in the IDC2 and ODC2 (2113, 2123...).
  8. Gamma : no hit in ODC1 and one or two in others (0111$\sim$0222).

  where four digit numbers denote the number of cell-hits in the ODC1, IDC1, IDC2, ODC2, respectively, and suffix 'p' means that a permutation of these numbers is allowed.

  A "number of hits generator" calculates the total number of cell-hits for each chamber and feed them into a "hit-pattern analyzer". The hit-pattern analyzer looks-up the ROM content and examine whether the hit-pattern belongs to any of the above categories. If the pattern is acceptable, a "scan-start" signal is sent to the scanner to initiate the rigidity analysis.

  Most of the shower events or empty JET events are rejected by this selection.

- Rigidity selection

  The events that have passed through the hit-pattern selection are then subject to the rigidity selection. All possible combinations of cell-hits are scanned and fed to the rigidity analyzer, which is the other half of the ROM look-up table. The output deflection is digitally compared to the seven threshold values, each of which corresponds to the hit-pattern category, except that the thresholds for Multi-clear and Multi-dirty are common. If the deflection is above some of the thresholds, i.e., the track has more negative deflection than the threshold, TT signals are generated. The resultant eight signals, which correspond to

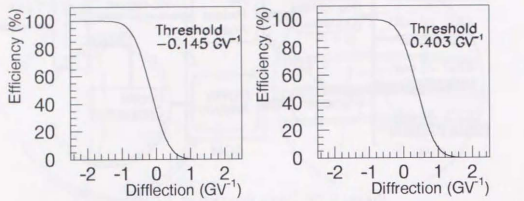

(a) Efficiency for antiprotons (b) Efficiency for antiheliums

Figure 2.26: Track trigger efficiency (a) for an $\bar{p}$ search (b) for an antihelium search.

the eight categories, are fed into the T1 trigger module to be combined with charge information from the TOF.

Figure 2.26 shows the efficiency of the rigidity selection as a function of deflection calculated by the simulation. The threshold values indicate the deflections where the efficiency become 50%. The left figure is for the threshold used for the $\bar{p}$ selection in the '93 flight. The right figure is for the threshold used for an antihelium selection. The curve for the $\bar{p}$ selection is set being shifted to the negative direction compared to that for the antihelium selection because a large number of protons should be cut more tightly by the rigidity selection.

T1 Trigger and Fast Clear

The TT only concerns the number of cell-hits and deflection of the track. The T1 trigger module combines the charge information from the T0 trigger module and the track information from the TT.

The T1 trigger module generates also unbiased trigger signals which bypass the TT selection. Each T1 trigger output reduced the number via a CD logic as is done in the T0 trigger module.

Finally the T1 trigger signal is generated as ORed signal of above twelve signals. If no T1 trigger signal is generated, a fast clear signal is sent to a "fast clear" module. The fast clear module sends the clear signal to all FADC and CAMAC modules and end up its task by unlocking the T0 module to accept the next event.

Table 2.4 summarizes a T1 trigger mode.

Table 2.4: Summary of T1 trigger

T1 Mode	T0 Trigger			CD	Trig rate[a]	Trig rate[b]
$\bar{p}$ clear	0	1	0	1/1	12 Hz	12 kHz
$\bar{p}$ dirty	1	1	1	1/1	18 Hz	18 Hz
$\bar{H}e$ clear	0	1	0	1/1	3 Hz	3 Hz
$\bar{H}e$ dirty	0	0	0	1/1	6 Hz	6 Hz
Missing	1	0	1	1/1	3 Hz	3 Hz
Multi clear	0	0	1	1/1	16 Hz	16 Hz
Multi dirty	0	0	0	1/1	8 Hz	8 Hz
Gamma	0	0	1	1/1	1 Hz	1 Hz
T0 Low CD	1	0	0	1/140	1.7 kHz	12 Hz
T0 High CD	0	1	0	1/40	500 Hz	12 Hz
T0 Gamma CD	0	0	1	1/100	50 Hz	0.5 Hz
T0 Ext CD	–	–	–	–	–	–

[a] Before count down
[b] After count down

2.6.2 Event Processing with Transputer

Figure 2.27 shows a block diagram of event processing. The shadowed boxes are transputers[1], each of which has a processing speed of 20 MIPS and a carrying out capability of parallel tasks with the hardware. Total 20 transputers are used in the FADC system, the CAMAC system, the event builder (EVB), and the transputer bank.

Each transputer is connected via a serial bus line "serial link", which has maximum transmitting rate of 1 Mbyte/s. Four links equipped in each transputer can be configured in a versatile and flexible manner to construct a complicated network.The command line and the event data line are divided in the most part of this system and the command can be received or issued while transmitting the event data. In addition, the rapid data transmittion is easily achieved since a link connects directly one transputer to another and there is no need for arbitration of the data way.

Thus, all transputers work concurrently and cooperatively to realize a fast event processing.

FADC System

The FADC system is comprised of a crate controller, fifteen FADC modules with total of 218 channels, and a compressor module.

The FADC modules read data from the JET chamber and the IDC, and convert them into 8-bit digit in the 35 ns sampling. The digitized data are successively

[1] product of INMOS corp.

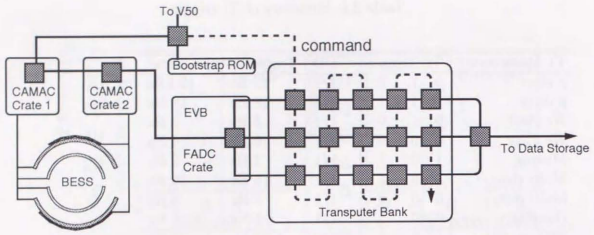

Figure 2.27: The block diagram of the data processing system using transputer network.

accumulated in the fast-in-fast-out (FIFO) after zero-suppression. The compressor module then reads, compresses and writes the data to another FIFO. The transputer controls the FADC and compressor modules. If the crate controller receives the T1 trigger signals, the transputer transfers the data from the FIFO to the EVB. Otherwise a fast clear signal is received and then all modules are reset to the initial state.

CAMAC System

The CAMAC system consists of two CAMAC crates. Each crate is controlled by an intelligent crate-controller, which employs a transputer inside. Thanks to transputer, two crate controllers can gather and transfer data in parallel at high speed.

In the crates, the following modules are installed and controlled by the crate-controller.

- Read-out electronics for the TOF counter and the ODC

  The discriminators, TDCs, and ADCs convert signals from the TOF and the ODC into the digital data.

- Trigger modules (T0, TT, T1)

  Trigger parameters such as CD numbers or TT thresholds are configured via CAMAC commands. The resultant trigger status can be read via CAMAC commands.

- 24-bit scalers

  Total 24-channel scalers count various trigger rates, which are used to monitor the trigger status and later used for the calculation of trigger efficiencies.

- Event-timing module

  An event-timing module includes a milli-second clock and measure the event-timing by 1-ms precision.

- Gate generators

  Gate generators are passive modules, i.e. , not controlled by CAMAC. They generate the gates with various widths and delays for use in other modules.

All data from above modules are transferred to the EVB via serial links.

Event Builder (EVB)

The data collected individually by the CAMAC and FADC system are fed to the EVB through the serial links. The EVB merges these data into the event structure. The event-building processes can be executed parallelly with the data-gathering process by the CAMAC and FADC crate-controller. The event data has a size of 1 kbyte typically and the EVB can handle them 1 kbyte per 1 ms, i.e., the maximum processing cycle of the EVB is 1 kHz. The built data are sent to the transputer bank for further processing.

Transputer Bank

The transputer bank receives the data from the EVB through three serial links. Fifteen transputers are arranged in a matrix way and process the event data simultaneously. All transputers execute the same program to process a event, which is flown from the up-stream to the down-stream. If the up-stream transputer is busy, the event data is passed to the down-stream transputer in sequencies.

The main role of the transputer bank is to clean up and sieve the event data using the whole detector information. Events with null data of the TDCs and small hits of FADC are removed here. The processes also reject events using inconsistency between IDC and ODC hits and TOF hits, events with less than 8 JET hits, and events with data sizes of more than 3 kbyte. About 2% event rate are reduced by these processes. Each transputer executes the above task in 20 ms and therefore the whole bank can accept the event rate of 1 kHz.

In addition to the filter process, one of the transputer makes various histograms concerning the filter processes. The resultant histograms are sent to the ground together with CAMAC scaler data in a second interval. These histograms are utilized to watch the status of the triggers and event filtering.

2.6.3 Data Storage

The data storage subsystem receives the data via OMNI-net and serial links. The event-, monitor-, and message-data from each subsystem are recorded into the 8-mm magnetic tape. Three transputers are employed for this task. The first transputer receives the command and the data from the OMNI-net and then sorts and transmits them into the second transputer through another link. The second transputer plays

a role as a buffer, which receives commands from one link and data from other two links, and send them to the third transputer though the last link. The third transputer interprets the commands and then controls a SCSI bus for recording the data. The maximum recording rate is 500 kbyte/s, which is limited by the SCSI bus transfer speed. The maximum storage capacity is 10 Gbyte in two tapes.

2.6.4 Communication

A communication subsystem manages communication between the payload and the ground station. The communication is carried out through the CIP, which provided by the national scientific balloon facility (NSBF). The commands to the DAQ are transmitted from the ground to the CIP via a radio link. The CIP converts the commands into 16-bit parallel data and send them to the communication subsystem. On the other hand, the message data and the event data are sent to the CIP via a serial line and then transmitted to the ground station through another channel of the radio link.

Although the maximum rate of transmittion to the ground is 10 kbyte/s, the event data are transferred by a rate of 0.1 Hz, i.e., 100 byte/s with some mergines. Commands are sent by a rate of 1 byte/s.

2.6.5 Monitor

A monitor subsystem handles the house-keeping data from the sensors. The monitor module has 64 individual differential-amplifiers and one analog-to-digital converter to digitize various sensor signals: temperatures (16 points), pressures (10 points), a magnet status (16 points), a chamber high voltage status (10 points), and a solar sensor and clinometers. The digitized data are transmitted to the ground station via the radio link and utilized to check the detector status during the flight.

Chapter 3

Data Samples

This chapter provides a general overview of data samples used in the present study. Section 3.1 describes the BESS '93 flight status. Section 3.2 summarizes the data samples taken in the flight. Section 3.3 explains the process method of the flight data. Section 3.4 describes the basic feature of the Monte Carlo method used in the present analysis.

3.1 Status of BESS '93 Flight

BESS was successfully launched by a balloon from Lynn Lake Manitoba in Northern Canada on Jul. 26 in 1993, which was a first scientific flight of BESS. The balloon of 29 Mf^3 lifted BESS into an altitude of 36.5 km (residual atmosphere 5 g cm $^{-2}$) and conveyed it to Peace River which located 1000 km east from Lynn Lake for 17 hours. During this level flight, a scientific data taking run are carried out for 13 hours. Total of 10^8 charged cosmic rays were triggered at T0 level and 3.6×10^6 of these triggers were recorded. After the scientific run, the balloon flight was terminated by cutting off balloon with the condition of both magnetic field and power off. The BESS detector are safely recovered by the next day. Figure 3.1 shows a balloon trajectory. The latitude varied from 56°48'N to 57°52'N while longitude from 101°25'W to 117°30'W. The corresponding cut-off rigidity varied from 0.34 GV to 0.43 GV.

Figure 3.2 illustrates a change of the magnetic field strength and typical temperatures during the flight. The temperature at the center of the detector varied between 10°C and 38°C. Figure 3.3 shows gravitational acceleration in the case of launching, termination , landing, and recovery. The maximum value of acceleration is 11.7 g in landing. With all rigorous operating conditions, no significant damage was observed both in the structure and in the performance according to the check after recovery.

3.2 Flight Data Sample

Trigger parameters (CD numbers and TT thresholds) were carefully adjusted to the design values using the data taken in the short pilot run just before the level

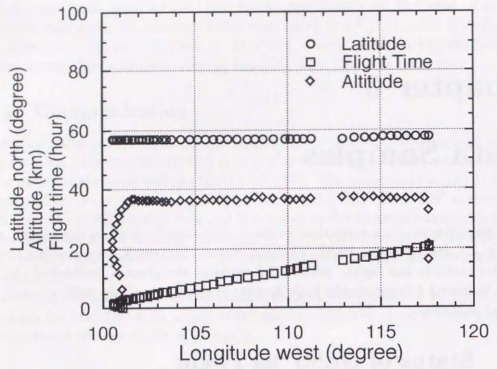

Figure 3.1: BESS '93 flight path in altitude, latitude vs longitude

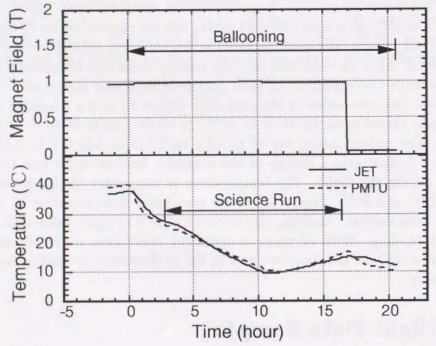

Figure 3.2: House-keeping data on magnetic field, temperature of TOF and Jet chamber.

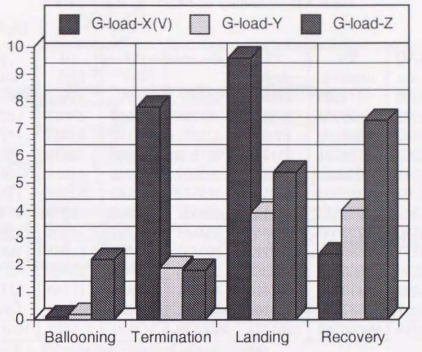

Figure 3.3: Acceleration loads during flight.

flight. One-third of the triggers were the unbiased events which bypassed the TT and two-thirds were biased events selected by the TT.

A dead time of the data taking was calculated to be 27 % from the scaler data. About two-thirds is due to the processing time of the fast clear. ($80\mu s \times 2.3$ kHz = 0.18). The other is resulted from the data gathering time. (1 ms × 90 Hz = 0.09). Total data acquisition time was 42389 s.

An online pedestal run was carried out to re-adjust the FADC threshold every 1 hour because the FADC module has a slight temperature dependence. In addition, all calibration parameters, such as a timing conversion gain or a chamber drift velocity, varies according to the drifts of the temperature and pressure. They have to be calibrated in a short interval. Thus all data samples are divided into 12 data set such that each data set includes at least 1 pedestal run.

Table 3.1 summarizes the number of data in each run. In the table, $T0_{nolock}$ denotes the number of the events triggered at T0 level. $T0_{lock}$ is the number of the T0 trigger that were locked out, i.e., the number of the initiation of the data acquisition. The right side of the table shows the breakdown of the recorded data, each of which corresponds to the T1 trigger mode (see Table 2.4).

3.3 Data Processing

The data recorded during the flight (RAW data) is composed of the event data, housekeeping data, command log, and message data in a compressed format. To

Table 3.1: Summary of BESS '93 flight data

run #	DAQ time	T0 nonlock	T0 lock	Record	T0 low	T0 high	$\bar{p}$ total	He total	others
13	3293	5819205	288681	284358	40914	41861	101362	28725	154271
14	2801	5819205	288681	241298	34913	35662	87358	24904	129036
15	3802	6695102	330457	325301	47113	48065	117514	32906	174881
16	2903	5108301	251336	247685	35968	36635	88783	24553	134349
17	3541	6246253	298337	293602	43980	44639	104476	28254	160872
18	4207	7382223	349531	343572	52182	52382	121234	32144	190194
19	4062	6929533	344137	339427	48913	48979	112146	27699	199582
20	4580	7723902	389954	383184	54747	54824	136519	36454	210211
21	3457	5889110	309112	303837	41524	41395	108311	30210	165316
22	2156	3665944	193283	189993	25899	25546	67299	19292	103402
23	3529	5410472	287415	314841	42436	41789	111536	32162	171143
24	4057	6887654	374161	368041	48532	47400	135373	39474	193194
total	42389	99666744	3661474	3635139	517121	519177	1291911	356777	950103

analyze the data and then search for $\bar{p}$'s among them, we should process the RAW data to extract physics properties of each event. For this purpose, we utilized a ZEBRA system [38] due to following reasons:

- The ZEBRA system provides a dynamic memory handling and enables to create the slots called BANK, which is useful to store many informations while processing.
- Data structure can be easily constructed hierarchically. We can develop the analysis routine for each detector according to the indivisual data structure.
- A data-base program (HEPDB) is available in the ZEBRA environment.

The first step of the data processing was to decompress and sort the RAW data and to convert them into the file with the ZEBRA format for event by event (STEP 1 in Fig 3.4) This file called a reformat (RFT) data has only DA bank which contains the entire RAW data and has size of 15 Gbyte. Using the RFT data, we performed a brief calibration of each detector and stored the resultant calibration parameters into data-base managed by the HEPDB program (STEP 2). In the next step (STEP 3), data were processed with a calibration data, creating several banks and filling with the event informations, such as hit positions or charges of the hits etc. This jobs were performed by each analysis routine corresponding to each detector. The resultant data structure is composed of following eight banks:

- DA bank – RAW data.

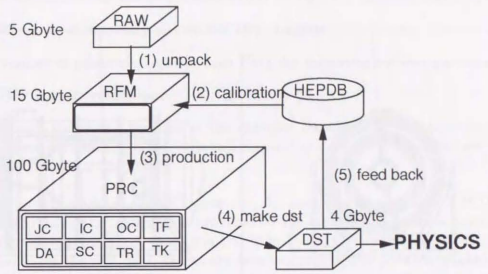

Figure 3.4: BESS data process method.

- TR bank – Trigger information of the events.
- JC bank – Event information concerning the JET chamber.
- IC bank – Event information concerning the IDC.
- OC bank – Event information concerning the ODC.
- TF bank – Event information concerning the TOF.
- SC bank – 24-channels of 24-bit scaler data.
- TK bank – Event properties using the whole detector information.

They were written into the zebra-formatted files as a processed (PRC) data, which amounts to the 100 Gbyte (STEP 3).

The PRC data contains all useful information for a physics analysis, however, its size is huge and costs of I/O handling are too high. The key informations were extracted from each bank and stored into the Data summary tape (DST) as a fixed width file (STEP 4). The main structure of the DST corresponds to the banks in the PRC data. Using the DST, detector performances were checked. If there were problems or improvements in calibration, then STEP $2 \sim 4$ were executed iteratively (STEP 5).

In the present study, the most physics analysis was done using the DST data.

3.4 Monte Carlo Simulation Sample

A Monte Carlo (M.C.) simulation is used in the present study for the following purposes:

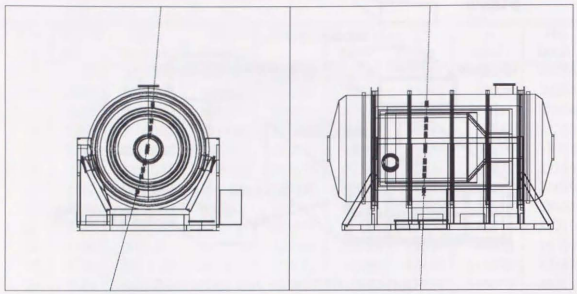

Figure 3.5: Simulated BESS detector

- The behavior of $\bar{p}$'s in the matter is different from those of protons primarily due to annihilation process. Some portion of $\bar{p}$'s will be lost through annihilation both in the atmosphere and in the detector. We use the M.C. simulation to correct this effect by simulating protons and $\bar{p}$'s both in the atmosphere and in the detector.
- In identifying $\bar{p}$'s, we rely mainly upon three key properties of the event; rigidity, $\beta \equiv (v/c)$, $\mathrm{d}E/\mathrm{d}X$. Due to interactions or accidental hits, some of them might be far from the expected value. In such cases, other particle species such as electrons might mimic $\bar{p}$'s. These faking processes and their probability should be investigated by the M.C. simulation as well as by the real data.

We built a simulated model of the BESS detector based on the GEANT code. Since we have assembled the simulated detector using the individual parts of the model which are defined with the precise dimensions and actual materials, the material distribution in the simulated detector accurately reproduced the real one. Figure 3.5 shows the view of the simulated BESS detector used in the event simulation.

In the analysis using the simulated events, we extracted the physics informations from the simulated detectors. Since the signals generated by the detector components include no measurement errors and statistical fluctuations, we smeared those signals with detector resolutions to reproduce the measured detector performance. We adjusted following parameters to reproduce the detector responses:

- Resolution of the position measurement by the JET chamber and IDC.
- Efficiency of detecting hits by the JET chamber.
- Number of photo-electrons in each PMT for minimum ionizing particles.
- TOF counter resolution.

Although the major features of the detector response are well reproduced by tuning these parameters, differences still remaine and affects the various selections as follows:

- In finding tracks in the JET chamber, the analysis program for the M.C. simulation uses the information provided by the GEANT code. This means that the efficiency of track finding is 100 % in the M.C. simulation. On the other hand, for the real data, tracks are searched among the possible combinations of hits in the JET chamber. Some of the tracks may not be identified as tracks, which causes decline of the track finding efficiency.
- There are extra hits in the real JET chamber that do not associate to any track. Some of them are due to so-called "after pulse" which produced by the electron diffusion. Some are the hits produced by the particle that was not be recognized as a track. The extra hits from these origins cannot be produced by the M.C. simulation and hence caused the difference of the selection efficiency.
- There are some electric-induced crosstalk in the IDC and ODC read-out electronics, which is not considered in the M.C simulation. This affects the cell-hit pattern of the IDC and ODC and consequently causes an inefficiency of the TT hit-pattern selection.
- We used the primary kinematics with only one particle in the M.C. study, however, some of the observed events include the another track that is apparently unrelated. Since we restrict the analysis to the event with the single track, these accidental track affects the efficiency of the selection.

These effects should be considered in the efficiency correction.

Chapter 4

Detector Performance

This chapter describes the detector performance in the BESS'93 flight. Section 4.1 provides an overview of measurement methods of rigidity, timing, and dE/dX. Section 4.2 describes the selection which are applied for a reliable and good performance of the detectors. The general performances are presented using the data samples which pass through the preselection in § 4.3

4.1 Measurement Method

4.1.1 Rigidity Measurement

A rigidity of the particle is measured by the JET and IDCs. First the transverse rigidity (R_t), i.e., the rigidity component perpendicular to the magnetic field direction is determined by a circular fitting in the $r\phi$ plane (Fig. 4.1 (a)). We use the following algorithms to eliminate the unconnected hits to the track in the fitting process.

1. Select good hits, which are defined as hits with enough charge and width, in the JET chamber and the IDCs.

2. Find tracks by connecting the good hits in the JET chamber and perform circular fitting using them.

3. Extrapolate the track to the IDC. If there are any good IDC hits near the extrapolated track, they are associated to the track.

4. Perform the circular fitting again using all hit points in the JET and IDCs which are associated to the track. We use a "KARIMAKI method"[40] for the fitting algorithm at this stage.

5. Scan all of good hits in the JET chamber and check if they are well near the track, i.e., within 5 times the distance of the position resolution. If the hit has a residual error of more than 5 σ, it is discarded. On the contrary, if the hits that are not yet associated to any track are laid within 5 σ from the track, it is added to the track.

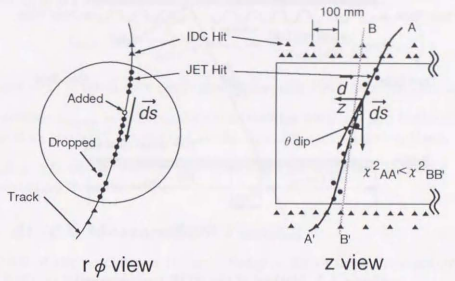

Figure 4.1: Method of the rigidity measurement.

6. Repeat step 4) and 5) twice.

The resultant R_t should be then corrected for non-uniformity of the magnet field of about 10%. From detailed study using M.C. simulation in the exact magnetic field, the correction using the simple function of the track position, path length, and mean strength of B field is found to be able to correct the rigidity within an accuracy of 1%.

To convert R_t into the total rigidity (R), we find the dip angle θ_{dip}, which is defined as an angle between the $r\phi$-component ($\vec{ds}$) and the z-component ($\vec{dz}$) of R, by fitting in the yz plane (Fig. 4.1). We use a similar iterative procedure as used in the $r\phi$ fitting to eliminate irrelevant hits. The selected hits are fitted to a sine-curve. Since the IDCs provide the only z positions modulo 100 mm, all possible combinations of the IDC hits are examined. The resultant θ_{dip} are obtained from the combination having minimum χ^2 value in the fitting.

Finally rigidity R are derived from R_t and θ_{dip} as,

$$R = \frac{R_t}{\cos\theta_{dip}}.$$

4.1.2 Time of Flight Measurement

Figure 4.2 illustrates the measurement scheme of time-of-flight (TOF). The TOF between top and bottom TOF hodoscopes is calculated for each track by the following procedure. We use here the suffix 'elec' for the PMT on the side of the electronics and the suffix 'tank' for the PMT on the side of the helium reservoir tank.

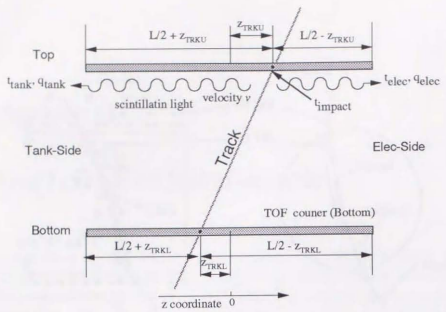

Figure 4.2: Method of the TOF measurement.

1. Correct a timing walk using the charge information for each PMT. We use following formula:

$$\hat{t_{elec}} = t_{elec} - a\sqrt{q_{elec}},$$

and

$$\hat{t_{tank}} = t_{tank} - a\sqrt{q_{tank}},$$

where $t_{elec,tank}$ is the measured timing, $\hat{t}_{elec,tank}$ the timing after the correction, q the measured charge of the PMT. Parameter a was determined by the beam test.

2. Derive the timing that the particle passed through the counter (t_{impact}) from the corrected timing of each PMT. Using the z-impact point (z_{trku}, z_{trkl}) of the particle which is calculated by extrapolating the combined track, t_{impact} is obtained for elec-side as,

$$t_{impact\_elec} = \hat{t}_{elec} - \frac{\frac{L}{2} - z_{trku,trkl}}{v_{eff}} - t_{offset}(z_{trku,trkl}),$$

and for tank-side as,

$$t_{impact\_tank} = \hat{t}_{tank} - \frac{\frac{L}{2} + z_{trku,trkl}}{v_{eff}} - t_{offset}(z_{trku,trkl}),$$

where v_{eff} is the effective light velocity in the counter and L is the length of the paddle. The second term is the propagation time for the scintillation light to reach to each PMT. The last term $t_{offset}(z)$ is the timing offset as a function of the z position. This is introduced to correct the velocity variation depending on the z position and is determined by calibration for each counter. Timing of both sides are then averaged with the weight as,

$$t_{impact} = \left(\frac{1}{\sigma_{elec}(z)^2} t_{impact\_elec} + \frac{1}{\sigma_{tank}(z)^2} t_{impact\_tank} \right),$$

where $\sigma(z)$ is the timing resolution of the each PMT as a function of z.

3. The value t_{impact} is individually calculated for both top and bottom counters, and then the TOF is obtained as the time difference between them.

The $\beta \equiv v/c$ of the particle can be determined from the TOF and the path length calculated from the track.

4.1.3 dE/dX Measurement

The dE/dX of the particles in the scintillator is derive from the measured charge by each PMT as following:

1. Subtract the pedestal value from the measured charge and correct the gain difference for each PMT.

2. Correct the z dependence of the signal amplitude due to the attenuation or loss of scintillation light using the z-impact position of the track. The detailed study in the beam test shows that the measured charge ($q_{measured}$) has the z-dependence as follows:

$$q_{measured} \propto a + be^{cz},$$

where a, b, c are parameters that should be determined by the calibration.

3. Average the charge of PMTs at both ends after the correction of step 2.

4. Divide the averaged charge by the path length in the scintillator through which the particle passed. This gives dE/dX in the TOF counters.

We finally normalize the dE/dX such that the mean value of the dE/dX distribtion for the minimum ionizing particles is unity.

4.2 Event Selection

The DST contains 3,635,139 events, including 517,148 "unbiased trigger sample" which were recorded for every 140th T0 trigger irrespective of the track trigger conditions. Among them there are some events which do not exhibit the proper performance to search for $\bar{p}$'s in certain reasons, such as the multi-track or interaction in the detector. We applied the selection prior to the analysis to ensure the good detector performance by rejecting those events.

4.2.1 Selection for Good Single Track

About half of the events exhibited either multi-tracks, or shower, or empty hit in the JET chamber. Following cuts were applied to reject these events and to select good single track events which passed through the fiducial region of JET chamber.

i) $N_{TOFU} = 1 \quad N_{TOFL} = 1$

There should be one and only one TOF counter hits in each of the top and bottom TOF scintillators.

ii) $N_{track} = 1$

Number of tracks found in the JET chamber should be one and only one.

iii) $N_{should} \geq 16$

where N_{should} is the number of the readout wires which the track should have passed in the JET chamber. This cut defines the fiducial region of the JET chamber and eliminates the track which scratches the outermost region, where the position measurement is less accurate than the central region due to the distortion of the electric field.

Total 2,160,082 events, including 221,898 unbiased trigger events, passed through this cut.

4.2.2 Track Quality Cut

Following cuts were then applied to ensure a good quality of the single track. The track were defined as the combined fit using hit points of the IDC and the JET chamber.

i) $N_{r\phi fit} \geq 13 \quad N_{zfit} \geq 5$,

where $N_{r\phi fit}, N_{zfit}$ are the number of JET hits used for the final track fitting in $r\phi$ and yz planes, respectively.

ii) $N_{trackhit} - N_{r\phi fit} < 7$,

where $N_{trackhit}$ is the number of JET hits associated to the track. This cut rejects the events which have too few good hits utilized in the combined fitting.

iii) $N_{totalhit} - N_{trackhit} < 20$,

where $N_{totalhit}$ is the total number of JET hits. This cut is to reject the events with too many extra hits which is not associated to the track.

iv) $\chi^2_{r\phi} < 4$, $\chi^2_z < 3.5$,

where $\chi^2_{r\phi}$ and χ^2_z are the reduced chi-square of the combined fitting in $r\phi$ and yz planes, respectively.

v) $N_{IDC1r\phi} \geq 1$, $N_{IDC2r\phi} \geq 1$ and
$N_{IDC1z} \geq 1$, $N_{IDC2z} \geq 1$.

This requires that at least one good hit in each of upper two and lower two layers of IDCs are used in the $r\phi$ and z fitting.

Figure 4.3 shows the histograms of these track-quality variables together with the cut positions. Open histograms are for the events that pass through the single-track selection, and the shadowed histograms are for the events that remain after the track-quality cut. Total 1,595,671 events, including 157,720 unbiased trigger events, passed through these cuts.

4.2.3 Selection Based on a Quality of the TOF Measurement

We heavily rely on the TOF measurement in identifying $\bar{p}$'s. The timing measurements might be disrupted by the accidental particle or by the local radio-active source which hit the TOF scintillator together with the cosmic ray particle.

To ensure a correct timing measurements, the following cuts on the TOF quality were applied at this stage.

i) $|z_{TRKU}| < 500$ mm , $|z_{TRKL}| < 500$ mm .

This requests that the extrapolated track should pass the fiducial z-region of TOF scintillators, which extend to $|z|$=550mm.

ii) In the $r\phi$ plane, the extrapolated track should pass through TOF counter.

iii) $|z_{TOFU} - z_{TRKU}| < 80$ mm , $|z_{TOFL} - z_{TRKL}| < 80$ mm .

This requires that z determined by the left-right time difference matches the z-impact point of the extrapolated track within the resolution of z_{TOF}.

Figure 4.4 illustrates the histograms of these variables together with the cut positions.

Open and shadowed histograms, respectively, are for the events which survived the single track selection and subsequently the track quality cut. Hatched histograms is for the events that passed through all of the TOF quality cut, too.

iv) $\Delta R_{A_{TOFU}} < 0.4$, $\Delta R_{A_{TOFL}} < 0.4$.

The ratio of the ADC values of the left and right phototubes (A_L, A_R) must be consistent with the z-impact position of the track. Figure 4.5-(a) shows the scatter plot of $\log(A_L/A_R) \equiv R_{ATOFU}$ versus the z-impact position. The line is the fit (7th-order polynomial) to the mean R values at each z bins. Figure 4.5-(b) shows the distribution of the residual R values (ΔR) around the fitted line versus z. The projected histogram of ΔR are shown in figure 4.5-(c) and (d) together with the cut positions($|\Delta R| < 0.4$).

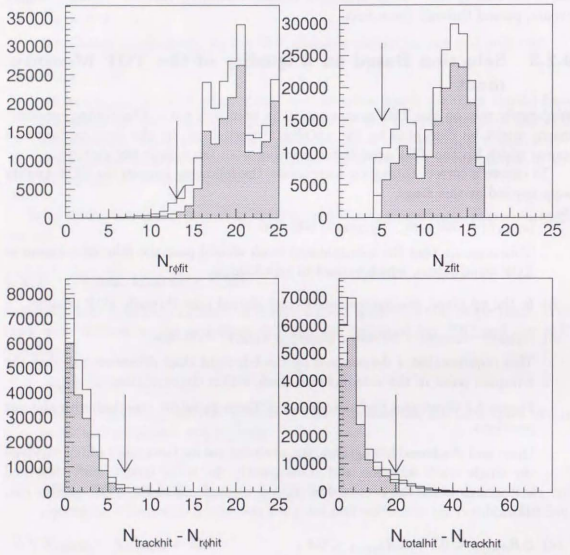

Figure 4.3: Track Quality Cut–1.

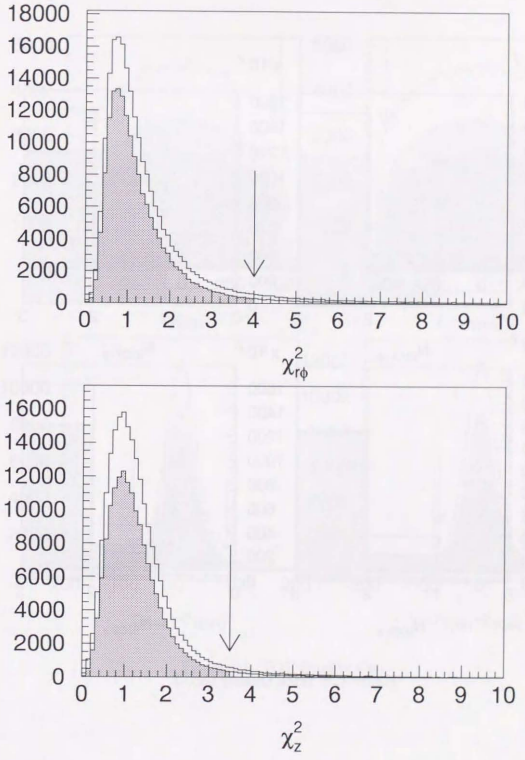

Figure 4.3: Track Quality Cut–2.

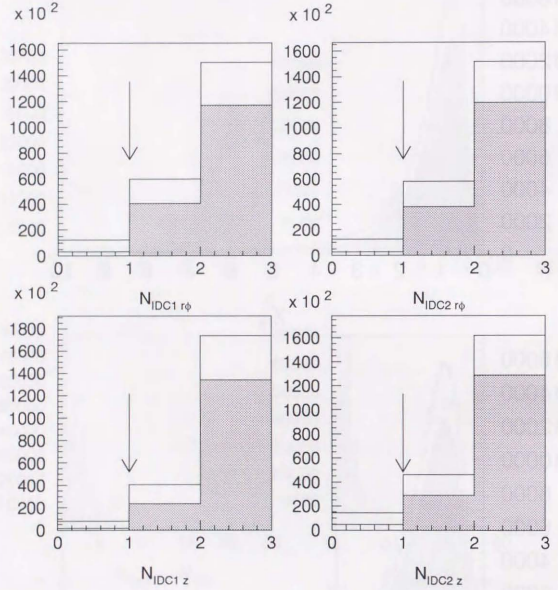

Figure 4.3: Track Quality Cut–3.

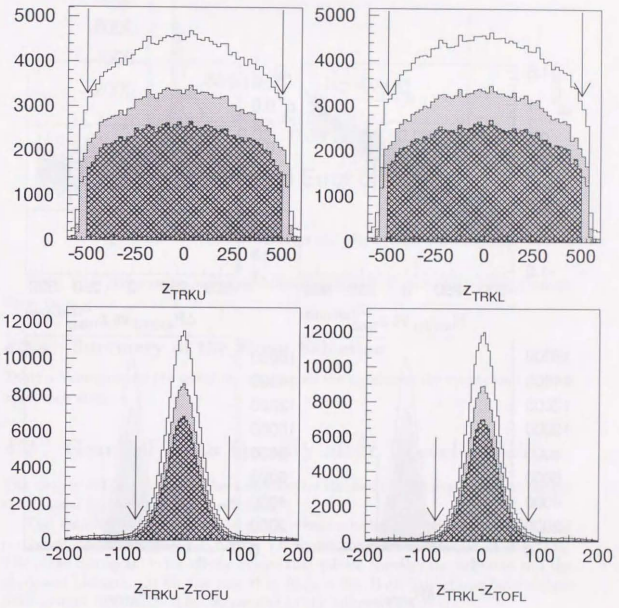

Figure 4.4: TOF Quality Cut.

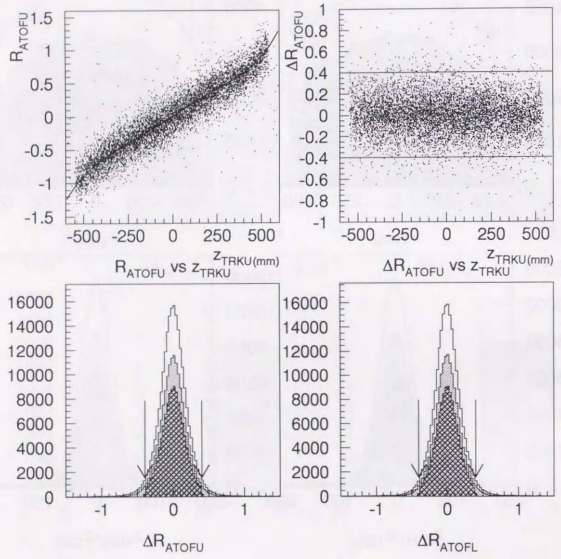

Figure 4.5: Selection by $R_{A_{TOF}}$.

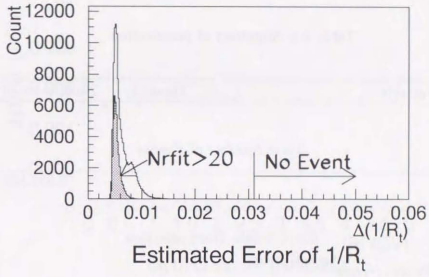

Figure 4.6: The estimated error of $1/R_t$ in the $r\phi$ fitting.

Total 1,167,350 events, including 115,562 unbiased trigger events, pass through these cuts.

4.2.4 Summary of the Event Selection

Table 4.1 summarizes the selection criteria and the number of the events that survive after each stage.

4.3 General Data Quality after Preselection

The quality of the detector performance can be checked by utilizing the event sample that passed through the above selection.

The estimated errors of the rigidity measurement were obtained in the final combined $r\phi$-fitting process. Figure 4.6 shows the estimated error of the $1/R_t$. The plane histogram is for all the events that passed through the selection and the shadowed histogram is for the case that $N_{rfit} > 20$. Both histograms have a clear peak around $\Delta(1/R_t) \sim 0.05$. According to the following relation,

$$\Delta\left(\frac{1}{R_t}\right) = \frac{\Delta(R_t)}{R_t^2} = \frac{\Delta(R_t)}{R_t}\,\frac{1}{R_t},$$

the $\Delta(1/R_t)$ is decomposed into fractional errors of rigidity ($\Delta(R_t)/R_t$) and inverse rigidity ($1/R_t$). The value of 0.005 thus indicates the particles with the transverse rigidity of up to 200 GV are at least 1σ away from the particles with the opposite charge. It is noted that no event with $\Delta(1/R_t)$ of more than 0.031 – were observed

Table 4.1: Summary of preselection.

Cut No.	Variable	Quantity	No.of events (unbiased)
	Total Number of Events		
			3,635,139 (517,148)
	Good Single Track selection		
1.....	N_{TOFU}, N_{TOFL}	1	
2.....	$N_{goodtrack}$	1	
3.....	N_{should}	≥ 16	
			2,160,082 (221,898)
	Track Quality Cut		
1.....	$N_{r-\phi-fit}$	≥ 13	
2.....	N_{z-fit}	≥ 5	
3.....	$N_{trackhit} - N_{r-\phi-fit}$	< 7	
4.....	$N_{tatalhit} - N_{trackhit}$	< 20	
5.....	χ^2_{r-phi}, χ^2_z	$< 4, < 3.5$	
6.....	$N_{IDC1_{r\phi}}, N_{IDC2_{r\phi}}, N_{IDC1_z}, N_{IDC2_z}$	≥ 1	
			1,595,671 (157,720)
	TOF quality Cuts		
1.....	$\lvert z_{TRKU}\rvert, \lvert z_{TRKL}\rvert$	$< 500\ mm$	
2.....	track should pass through the counter in rϕ plane		
3.....	$\lvert z_{TOFU} - z_{TRKU}\rvert, \lvert z_{TOFL} - z_{TRKL}\rvert$	$< 80\ mm$	
4.....	$\Delta A_{TOFU}, \Delta A_{TOFL}$	< 0.4	
5.....	T_{TOFL}	$< 1.5\ ns$	
			1,167,350 (115,562)

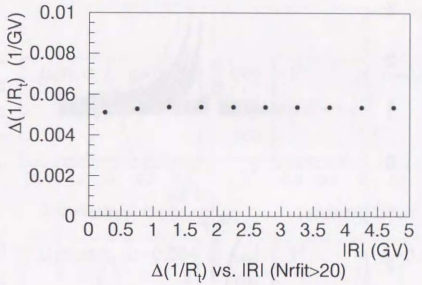

Figure 4.7: $\Delta(1/R_t)$ as a function of the absolute rigidity.

and therefore all events with rigidity below 1 GV are more than 30σ away from the negative rigidity region. Figure 4.7 shows the mean of the $\Delta(1/R_t)$ distribution as a function of the absolute rigidity for the case that $N_{rfit} > 20$. Almost constant values are obtained in the entire rigidity range.

The quality of the TOF and β measurement can be checked by utilizing the unbiased trigger sample. Figure 4.8 (a) and (b) show β^{-1} versus rigidity plot for the unbiased trigger sample and the M.C. data sample, respectively. The M.C. data are produced by isotropically injecting the protons having the same rigidity spectrum into the simulated BESS detector. Distribution of the particles including albedo are well reproduced in the M.C. data except for the energetic electron, He, and isotopes of proton. It is clear from both figures that the down going particles in the positive β^{-1} region are unambiguously separated from the up-going albedo particles in the negative β^{-1} region. Various particles can be clearly identified up to the rigidity of a few GV. Figure 4.9 shows the resolution of β^{-1} measurement at various rigidity bins. The r.m.s. resolution of about 0.05 and 0.06 are obtained for protons and muons/pions/electrons, respectively. Two independent measurement errors contribute to the resolution of β^{-1} as follows:

$$\frac{\Delta\beta^{-1}}{\beta^{-1}} = \frac{\Delta t}{t} + \frac{\Delta\ell_{path}}{\ell_{path}},$$

where t is the measured TOF and ℓ_{path} is the path-length of the particle between the top and the bottom TOF counter. Figure 4.10 shows fractional $1/\beta$ resolution as a function of β for the unbiased data and the M.C. data. The open boxes in the figure are for the real data and the black dots are for the M.C. data. Both exhibit

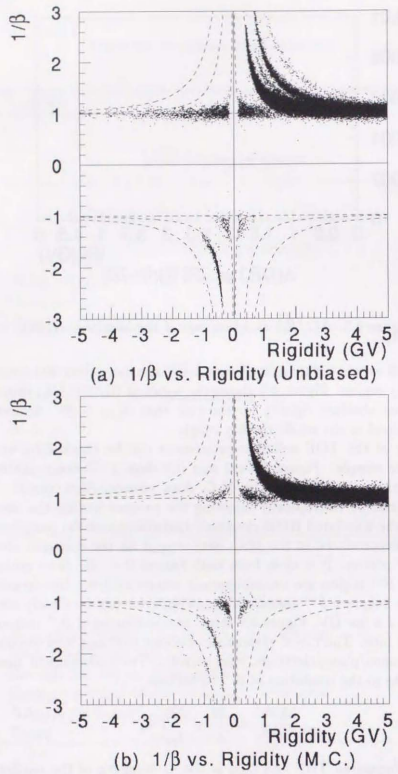

Figure 4.8: $1/\beta$ vs Rigidity of (a) unbiased data sample and (b) M.C. data sample.

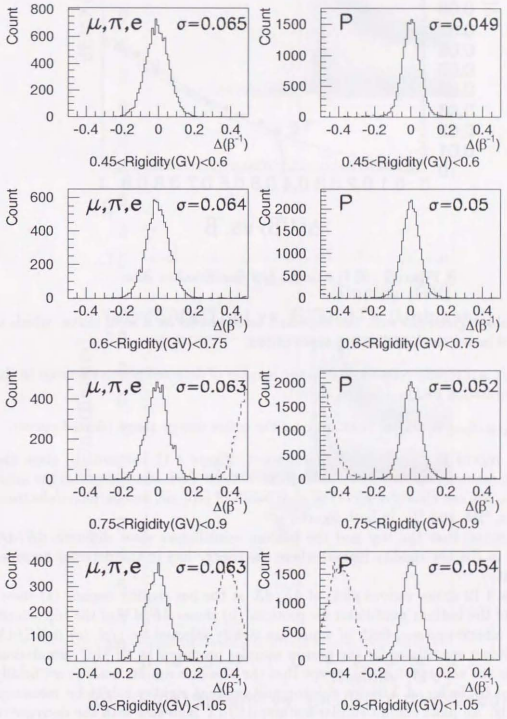

Figure 4.9: Distribution of $1/\beta$.

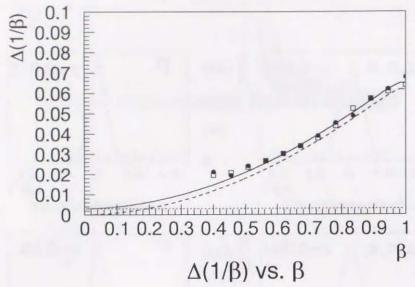

Figure 4.10: Fractional $1/\beta$ resolution vs *beta*.

a reasonable agreement with the expected value shown as a solid curve, which is calculated based on the following assumptions.

- $\Delta t/t$ is inversely proportional to the number of detected photo-electrons in the scintillation paddle (dashed curve).
- $\Delta\ell_{path}/\ell_{path}$ is almost constant over the entire energy range (dotted curve).

With regard to the dE/dX measurement, Figure 4.11 (a) and (b) show the dE/dX measured respectively by the top and bottom TOF scintillators for the unbiased data. We can clearly observe the clear bands of protons, muons/pions/electrons deuterons, ^{3}He, and ^{4}He in both figures.

It is noted that the top and the bottom scintillators show different dE/dX behavior in the low rigidity region, where the energy loss in the detector becomes significant.

Figure 4.12 shows various plots of dE/dX at the low rigidity region: (a) shows dE/dX of the bottom scintillator for protons, (b) shows dE/dX of the top scintillator for albedo-protons, both of which are tightly selected by $1/\beta$, (c) is dE/dX of the bottom scintillator for the proton samples produced by th M.C. simulation, and (d) is the same plot as (c) except that the absolute rigidity scale is artificially multiplied by factor of 1.03 for the supposition that rigidity might be measured incorrectly. All plots exhibit similar feature; dE/dX increases with the decrease of rigidity and steeply falls down around the rigidity of 0.45 GV. This indicates that the proton with the rigidity below 0.45 GV loose most or all kinetic energy while passing through the material between the TOF counter and the central detector.

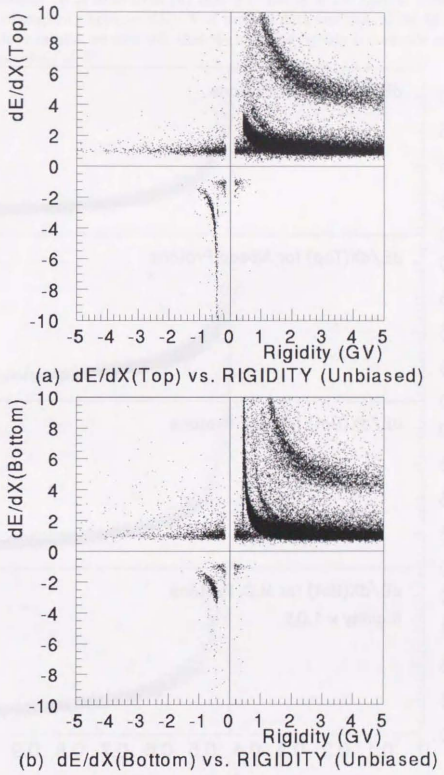

Figure 4.11: dE/dX of the Unbiased Sample and M.C. sample

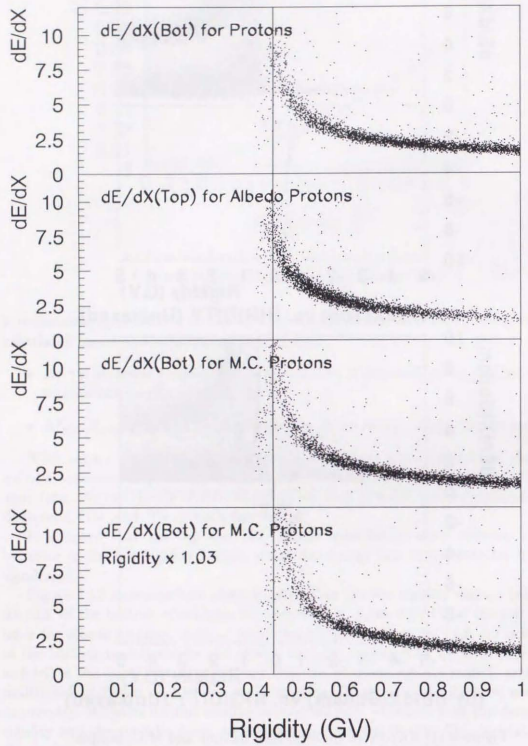

Figure 4.12: dE/dX of the stopped protons.

This feature is sensitive to the rigidity scale and can be utilized to check the rigidity measurement. It is clear from (d) that 3% change of the rigidity scale causes significant discrepancy between dE/dX of the real data and that of the M.C. data. Based on these results, we conclude that the absolute rigidity is correctly measured within an accuracy of 3%.

Chapter 5

Search for Antiprotons

This chapter provides the analysis to search for $\bar{p}$'s using the BESS'93 flight data. After the preselection for events with the good detector performance, the dE/dX cut is applied to extract proton and $\bar{p}$ signals in § 5.2. Section 5.3 describes the method of albedo rejection which separate down-going particles from up-going particles. Section 5.4 provide identification of protons and $\bar{p}$'s using their mass-square. Observed $\bar{p}$'s are closely examined in § 5.5. In the last section, we consider the possible background processes.

5.1 Preselection

Before search for $\bar{p}$'s, preselections described in § 4.2 are applied. This rejects potential backgrounds due to the mis-measurement of the rigidity or TOF.

5.2 Selection by dE/dX

We utilize a band structure of dE/dX to extract only protons and $\bar{p}$'s among other species. Figure 5.1 shows dE/dX-versus-rigidity plots of the top and the bottom scintillators for a pure proton sample, which is selected by cutting tightly on β. The central line corresponds to the peak of the dE/dX distribution. The dashed lines define the "proton dE/dX-band". We require that $\bar{p}$'s as well as protons must have the dE/dX in this "proton dE/dX-band".

Figure 5.2 shows histograms of dE/dX-spread around the proton peak which corresponds to the central line of Fig. 5.1. The arrows in the figures represent the positions of the "proton dE/dX-band". The dashed histograms are for muons/pions/electrons. The requirement to be in the "proton dE/dX-band" (dE/dX cut) rejects most of muons/pions/electrons and all of the particles with the charge greater than 1, while keeping 90% of protons at each rigidity bins.

Figure 5.3 (a) and (b) show β^{-} vs rigidity for all events that passed through the preselection: (a) is the plot for the samples before the dE/dX cut and (b) is for the samples after the cut. Compared to (a), most of the muons/pions/electrons in the rigidity below 1 GV are eliminated in (b) as well as deuterons and heliums.

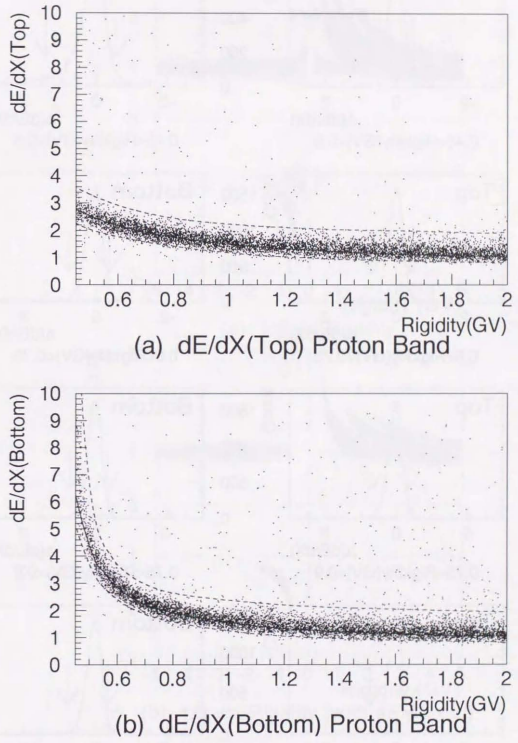

Figure 5.1: Proton dE/dX-band

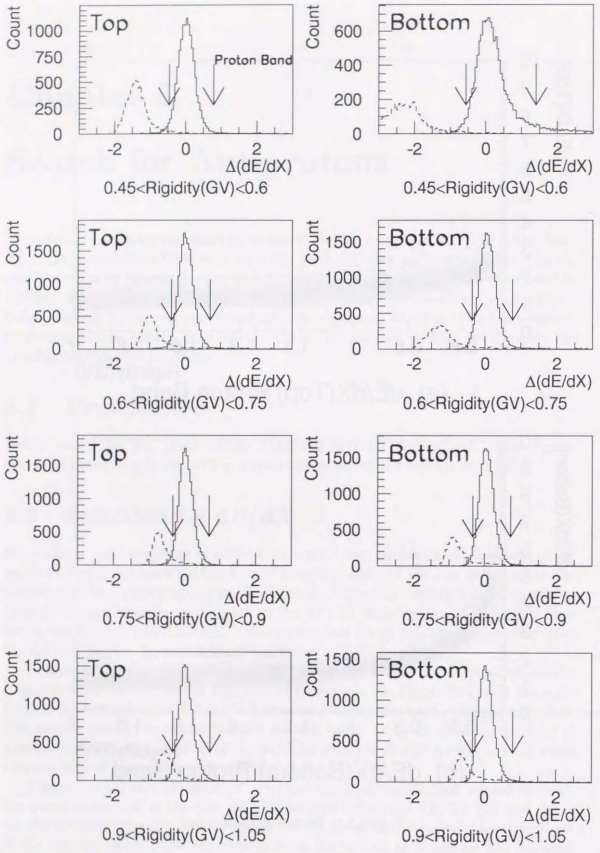

Figure 5.2: $\mathrm{d}E/\mathrm{d}X$ spread around the proton $\mathrm{d}E/\mathrm{d}X$ peak. Arrows represent the positions of the $\mathrm{d}E/\mathrm{d}X$ cut in each rigidity bin.

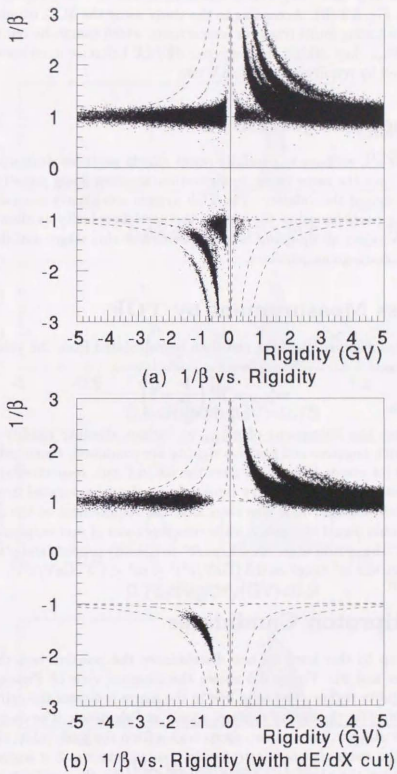

Figure 5.3: β^{-} vs rigidity for all event samples (a) before $\mathrm{d}E/\mathrm{d}X$ cut and (b) after $\mathrm{d}E/\mathrm{d}X$ cut.

It is also noted that off-timing events scattered in the $\beta^{-1} < 1$ region are clearly sweeped out in Fig. 5.3-(b). According to the study using the M.C. simulation, all of them are events having multi-tracks or interactions, which cannot be removed by the preselection. Since they exhibit the improper dE/dX behavior in either scintillator, they are rejected by requiring the dE/dX cut.

5.3 Albedo Rejection

In searching for $\bar{p}$'s, we have to carefully reject albedo particles since up-going positive particles have the same event configuration as down-going negative particles except for the sign of the velocity. The TOF system can clearly separate up-going and down-going particles using the sign of the particle-velocity as shown above in Fig. 5.3(b). We reject all up-going albedo particles at this stage, and limit further analysis to the down-going particles.

5.4 Mass Measurement by TOF

The mass of the observed particles can then be calculated from the velocity β and the rigidity R as

$$m^2_{TOF} = R^2 \left(\frac{1}{\beta^2} - 1 \right).$$

Figure 5.4 shows the histograms of m^2_{TOF} at various absolute rigidity ($|R|$) bins, where events with negative and positive rigidity are combined. Open and shadowed histograms are for events before and after the dE/dX cut, respectively. The sharp peak of the proton is visible at every rigidity bins, clearly separated from the peak of muons/pions/electrons. It is also clear that the requirement of the dE/dX cut extracts the proton signal efficiently, while rejecting most of muons/pions/electrons. We define here "the proton mass square range" to identify protons and $\bar{p}$'s for further analysis. We set the m^2 range as $0.5\ (\mathrm{GeV}/c^2)^2 < m^2 < 1.3\ (\mathrm{GeV}/c^2)^2$.

5.5 Antiproton Candidates

All selections up to this level do not discriminate the positive and the negative rigidity (proton and $\bar{p}$). Figure 5.5 shows the close-up view of Figure 5.3-(b) in the *negative* rigidity region. The solid line in the figure indicates the calculated β^{-1} curve from rigidity for the case of protons, pions, and electrons. The dashed and the dotted line indicates the one and two sigma region from the peak value, respectively. The peak for the muons/pions/electrons are coming into the 5 σ region from the proton peak above the absolute rigidity of 1.05 GV. *We thus restrict ourselves to the absolute rigidity range between 0.45 GV and 1.05 GV for further analysis.* The lower limit bound is set to reject the events that stop in the bottom scintillator.

Four events (stars) are observed near the $\bar{p}$ line clearly apart from the muon/pion/electron region in Fig. 5.5.

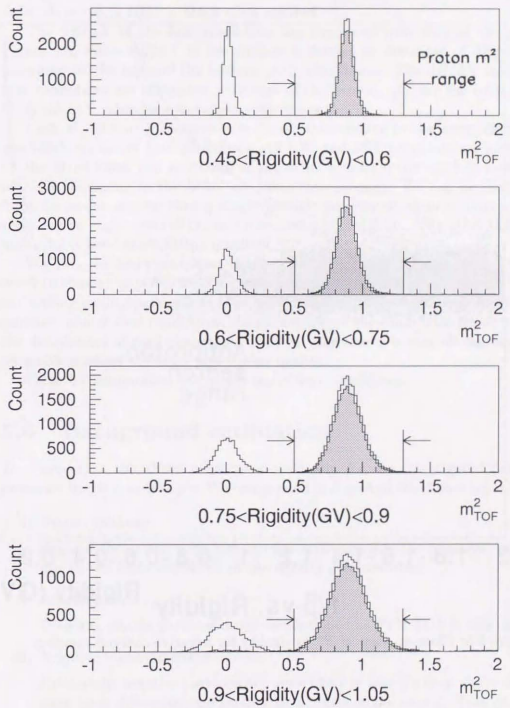

Figure 5.4: m^2_{TOF} distribution.

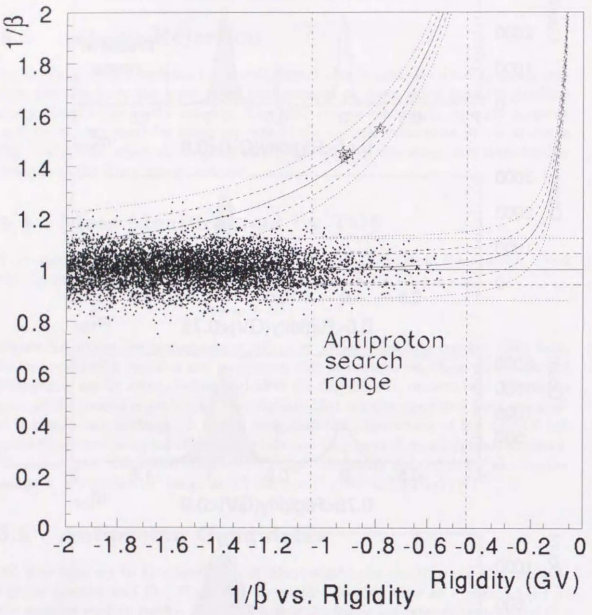

Figure 5.5: Close-up view of β^{-} vs rigidity for negative-charged samples.

Figure 5.6 shows m^2_{TOF} histograms for *negative* rigidity events after the $\mathrm{d}E/\mathrm{d}X$ cut. The dashed histograms are just to indicate the position of the $\bar{p}$ peak. We observed four $\bar{p}$ candidates (one at $0.75\mathrm{GV} < -R < 0.9\mathrm{GV}$ and three at $0.9\mathrm{GV} < -R < 1.05\mathrm{GV}$), well separated from the cluster of muons/pions/electrons.

Figure 5.7 shows the close-up view of the m^2_{TOF} distribution. All four $\bar{p}$ candidates show m^2_{TOF} right at the $\bar{p}$ mass squared.

The $\mathrm{d}E/\mathrm{d}X$ of the four candidates are compared with that of the proton in Figure 5.8, where $\mathrm{d}E/\mathrm{d}X$ of the particle is defined as the mean of $\mathrm{d}E/\mathrm{d}X$ values measured by the top and the bottom TOF scintillators. The $\mathrm{d}E/\mathrm{d}X$ values of the four candidates are consistent with that of the proton, and are far from the most likely $\mathrm{d}E/\mathrm{d}X$ value for muons/pions/electrons.

Each of the four $\bar{p}$ candidates is closely investigated in the event display. Figure 5.9 shows one of four candidates. All IDC and JET hit points are located right on the fitted track and deviation of the ODC hits from the track is reasonable if multiple scattering in the MAG are taken into account. We can be fairly certain from the event display that a single particle penetrated without interaction and there are no slight signs of the mis-measurement of rigidity. The other three events also exhibit good track-fitting qualities.

We also checked parameters used in the preselection for all candidates. Figure 5.10 shows the position of the candidates in the histogram of the track quality and timing quality parameters. The histograms with darkest hatch indicate the parameter value of four candidates. All parameters of the candidates reside well inside the distribution of each histogram. Thus we may conclude that all candidates have no problem about the track and timing quality.

Table 5.1 summarizes the properties of four candidates.

5.6 Background estimation

To ensure that the above candidates are really $\bar{p}$'s, we investigated background processes which may fake $\bar{p}$'s. We categorized background into following three cases:

i) Proton spillover

Some of the proton with high rigidity spill over onto the negative rigidity side due to the finite resolution of the rigidity measurement.

ii) Albedo proton

Up-going albedo particles might be identified as $\bar{p}$'s if TOF is mis-measured.

iii) Negative muons/pions/electrons

Relativistic negative particles are more likely to fake $\bar{p}$'s than above two cases, since time differences are smaller than those in the case 2. This case should be considered most closely.

For above three cases, we examined likelihood of background production using the real data and the M.C. data.

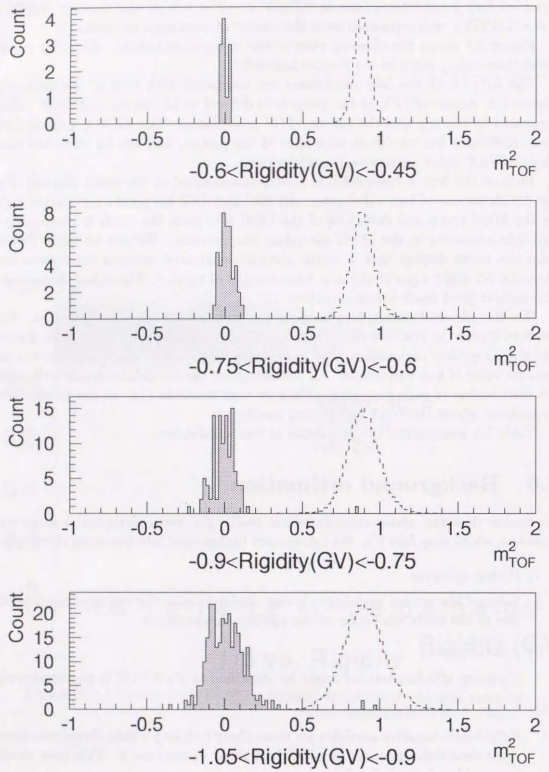

Figure 5.6: m^2_{TOF} distribution (negative rigidity).

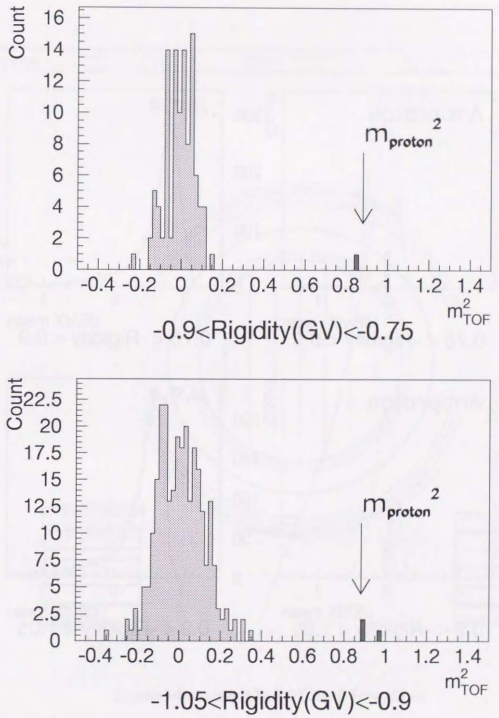

Figure 5.7: m^2_{TOF} distribution of the $\bar{p}$ candidates.

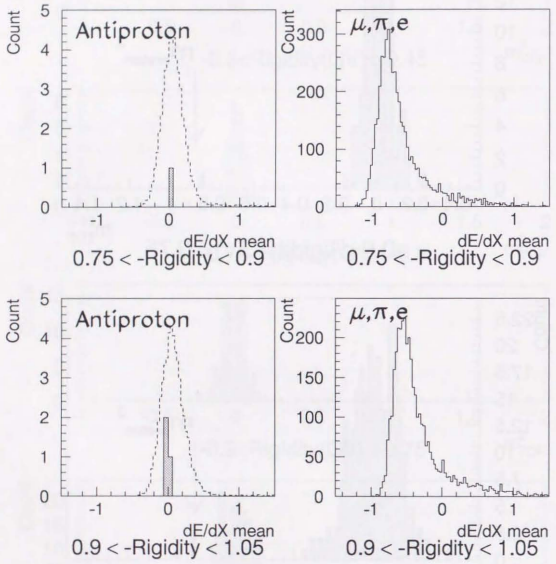

Figure 5.8: dE/dX of the $\bar{p}$ candidates.

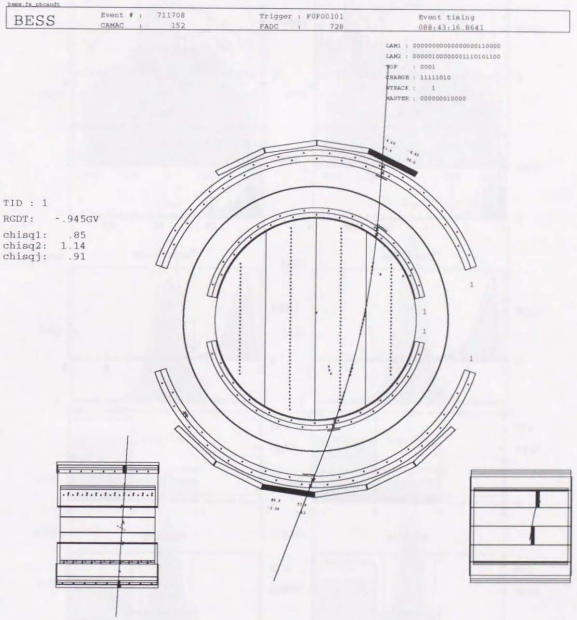

Figure 5.9: Event display of the $\bar{p}$ candidates.

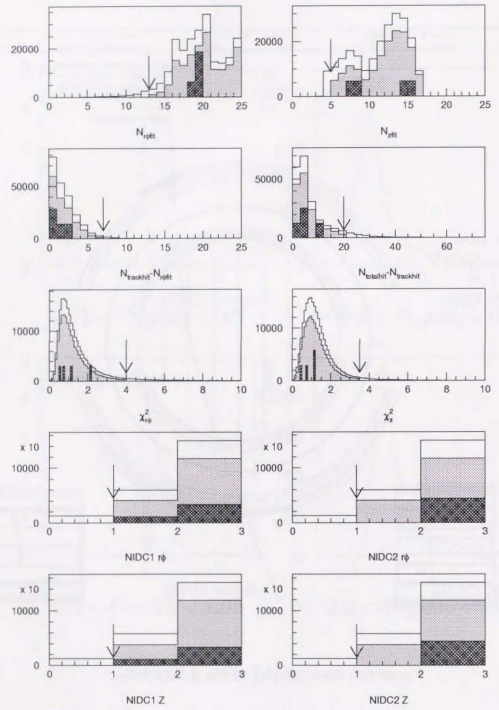

Figure 5.10: Track and timing quality parameters for $\bar{p}$ candidates –1.

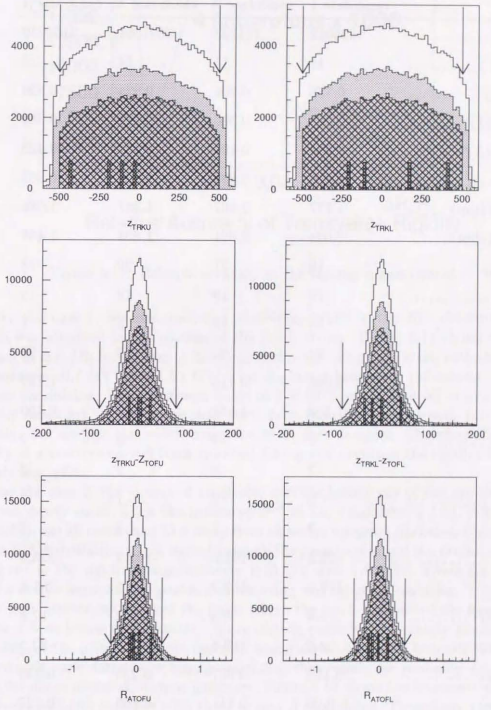

Figure 5.10: Track and timing quality parameters for $\bar{p}$ candidates –2.

Table 5.1: Properties of $\bar{p}$ candidates.

	candidate 1	candidate 2	candidate 3	candidate 4
Evt #	1695042	711708	3597064	3164639
Run #	18	15	24	22
Rigidity	0.786	0.904	0.924	0.930
KE(DET)[a]	0.285	0.365	0.378	0.383
KE(TOA)[b]	0.334	0.407	0.423	0.425
M^2_{TOF}	0.860	0.893	0889	0.963
dE/dX(top)	1.777	1.407	1.387	1.680
dE/dX(bot).....	2.034	2.021	1.854	1.468
$N_{trackhit}$	19	21	20	18
$N_{r\phi fit}$	19	19	19	18
n_{zfit}	14	15	8	7
$N_{totalfit}$	24	25	30	20
$\chi^2_{r\phi}$	0.596	0.715	2.103	1.142
χ^2_z	1.198	1.144	0.763	0.450
$N_{idc1r\phi}$	1	2	2	2
$N_{idc2r\phi}$	2	2	2	2
N_{idc1z}	2	2	1	2
N_{idc2z}	2	2	2	2
z_{TRKU}	-22.5	-191.8	-102.9	-423.9
z_{TRKL}	173.3	-117.3	411.1	-201.8
Δz_{TOFU}	1.8	5.3	27.2	-17.6
Δz_{TOFL}.....	2.0	-19.4	43.6	-33.5
ΔR_{TOFU}	-0.120	-0.037	0.235	0.039
ΔR_{TOFL}	0.00	-0.111	-0.169	0.127

[a]kinetic energy measured at the detector center (GeV)
[b]kinetic energy at the top of the atmosphere (GeV)

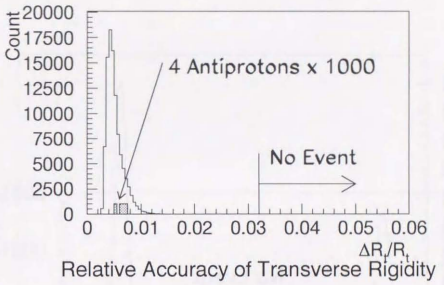

Figure 5.11: Relative accuracy of the rigidity measurement.

For the case 1, we examined the relative accuracy in the R_t^{-1} determination, which was obtained in the process of the track fitting. Figure 5.11 shows the histogram of $\Delta R_t/R_t$ for all events that passed through the preselection with the rigidity between -0.7 GV and -1.05 GV. The shadowed histogram indicates the value of four candidates. The maximum value of 3×10^{-2} means that all events in this rigidity range are located more than 30 σ away from the protons with the infinite rigidity. We confirm this result using the M.C. data samples. Therefore the probability of a positive-curved track (proton) faking any events in the rigidity range is utterly negligible.

For the case 2, the chance of an albedo particle faking any of the candidates is also extremely small, since the measured β^{-1} of the candidates (1.54, 1.45, 1.44, and 1.42), are all more than 45 σ away from those for up-going particles. Figure 5.12 shows β^{-1} distribution which passed through the preselection and the proton dE/dX band cut in the rigidity range between -0.75 GV and -1.05 GV. There are no tail for the events between two peaks of down-going and up-going particles. To confirm this result further, we checked the point where the track intersected the base plane at the 1.5 m below the detector. Since albedo particles are mainly produced in collisions of the primary cosmic-ray with materials which reside beneath the BESS detector, if candidates were albedo particles, they would be probably originated from the dense material, such as batteries. Figure 5.13 shows the intersection points of albedo particles together with those of four $\bar{p}$ candidates. Three large rectangles are drawn to indicate the position of the battery containers. Size of the squares is proportional to the event population. It can be clearly seen that most albedo particles are coming from the batteries while all of the candidates (black stars) are well apart from the batteries.

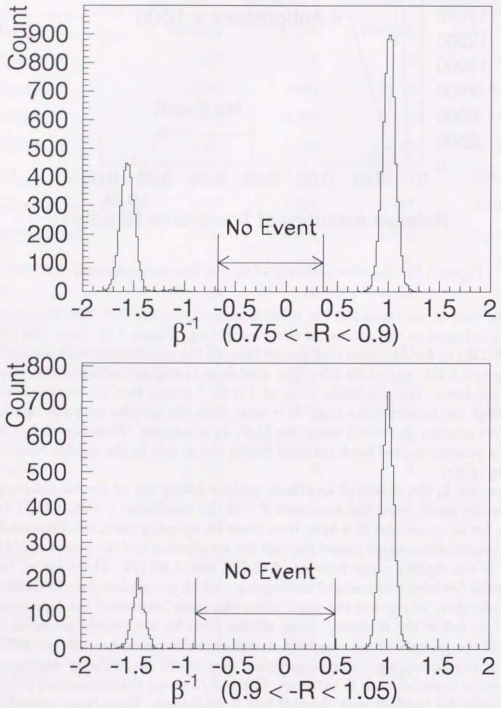

Figure 5.12: β^{-1} distributions for negative-charged particles before $\mathrm{d}E/\mathrm{d}X$ cut.

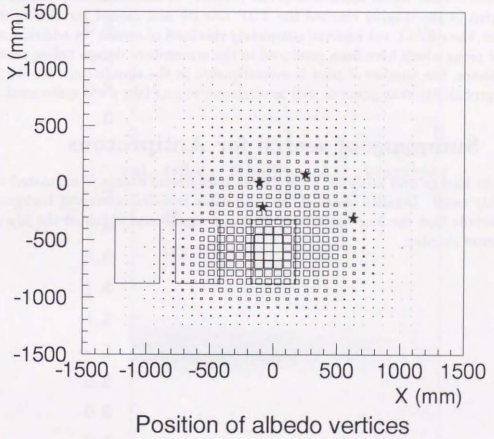

Figure 5.13: Intersection point of albedo particles and the BESS base plane.

For the case 3, all four candidates are located more than 6 σ away from the electron/muon/pion peak. However, the possibility remains that they are mis-identified electrons/muons/pions which have moved far from their response curve by some interactions or accidental hits. We utilized the M.C. simulation to evaluate this likelihood and its origin. Since our detector have no ability to distinguish the electron/muon/pion in most of the search range, we tested for all species by generating simulated events more than five times as many as observed negative-charged events. Some of the result are shown in Fig. 5.14. No events are observed inside the proton 2 σ lines for all samples after the dE/dX cut, although some of pions before the dE/dX cut come into the proton 2 σ range. We examined these events closely and have found that they all have interactions in the detector. Figure 5.14 shows one of the events, which interacted in the magnet. A slow secondary proton from the vertex in the magnet reached the TOF counter and caused the timing delay. However, the dE/dX cut rejected completely this kind of events. In addition, since most of pions which have been produced in the atmosphere decays before reaching the detector, the number of pion is overestimated in the simulation. We conclude that a probability that pions as well as electrons/muons fake $\bar{p}$'s is quite small.

5.7 Summary of search for Antiprotons

From the background analysis, a number of background events is estimated to be negligibly small. Detailed check of the candidates revealed no sign of background. We conclude that the four candidates are the $\bar{p}$ signals and obtained the $\bar{p}/p$ ratio in the next chapter.

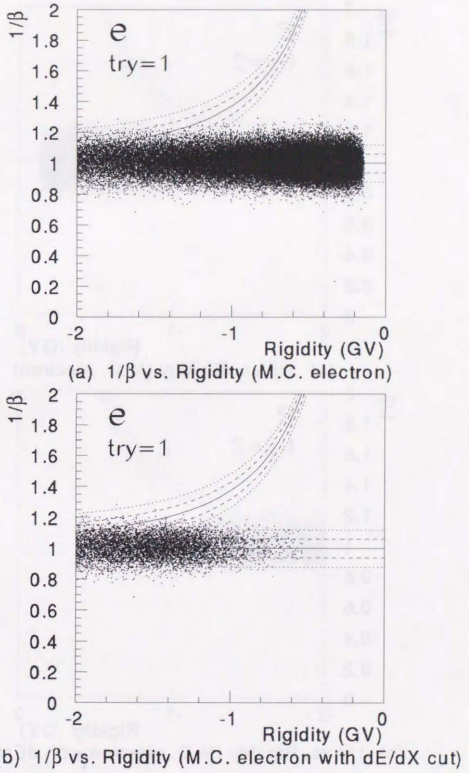

Figure 5.14: β^{-} vs rigidity for M.C. electron (a) before dE/dX cuts and (b) after dE/dX cut – Try-1.

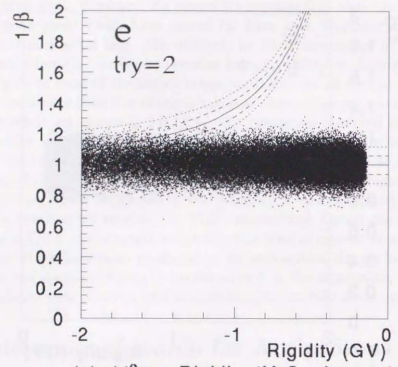

(a) 1/β vs. Rigidity (M.C. electron)

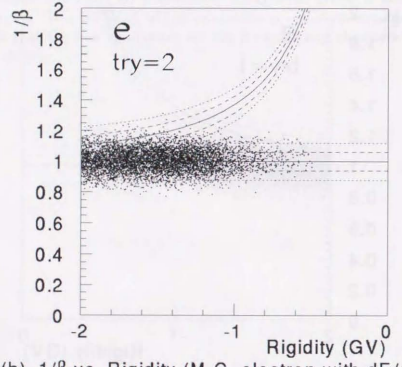

(b) 1/β vs. Rigidity (M.C. electron with dE/dX cut)

Figure 5.14: β^{-} vs rigidity for M.C. electron (a) before $\mathrm{d}E/\mathrm{d}X$ cuts and (b) after $\mathrm{d}E/\mathrm{d}X$ cut – Try-2.

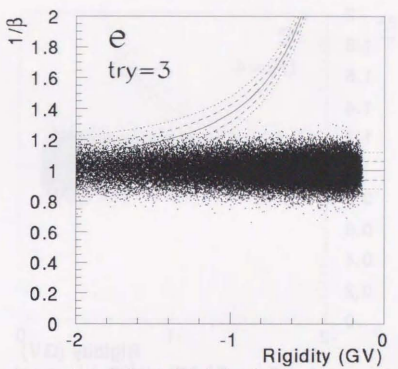

(a) 1/β vs. Rigidity (M.C. electron)

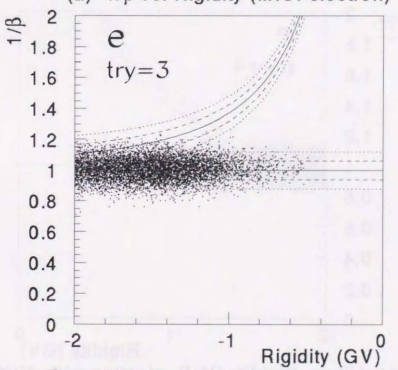

(b) 1/β vs. Rigidity (M.C. electron with dE/dX cut)

Figure 5.14: β^{-} vs rigidity for M.C. electron (a) before $\mathrm{d}E/\mathrm{d}X$ cuts and (b) after $\mathrm{d}E/\mathrm{d}X$ cut – Try-3.

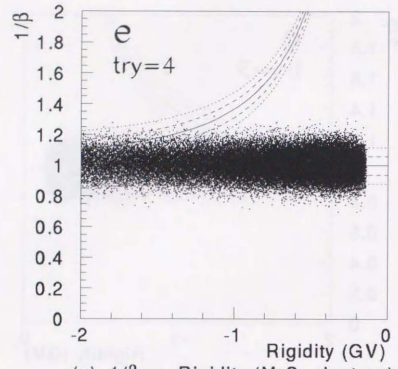

(a) 1/β vs. Rigidity (M.C. electron)

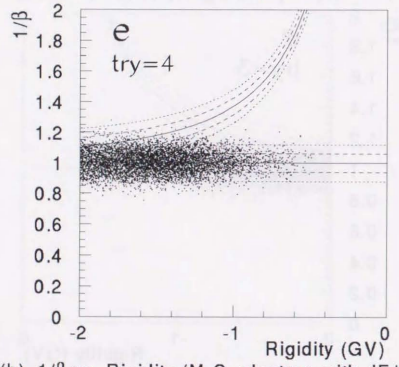

(b) 1/β vs. Rigidity (M.C. electron with dE/dX cut)

Figure 5.14: β^{-} vs rigidity for M.C. electron (a) before $\mathrm{d}E/\mathrm{d}X$ cuts and (b) after $\mathrm{d}E/\mathrm{d}X$ cut – Try-4.

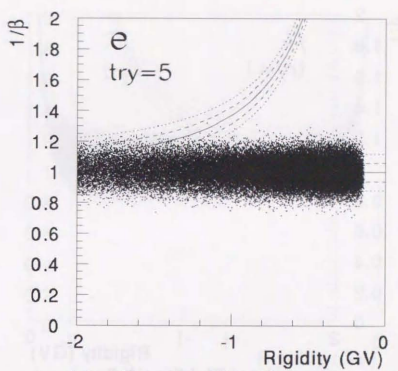

(a) 1/β vs. Rigidity (M.C. electron)

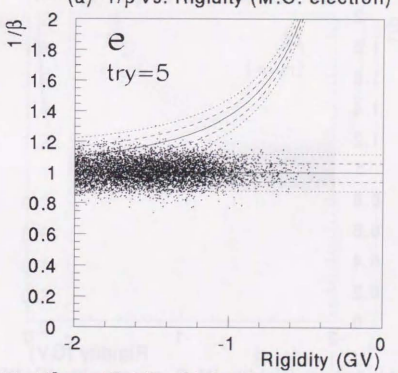

(b) 1/β vs. Rigidity (M.C. electron with dE/dX cut)

Figure 5.14: β^{-} vs rigidity for M.C. electron (a) before $\mathrm{d}E/\mathrm{d}X$ cuts and (b) after $\mathrm{d}E/\mathrm{d}X$ cut – Try-5.

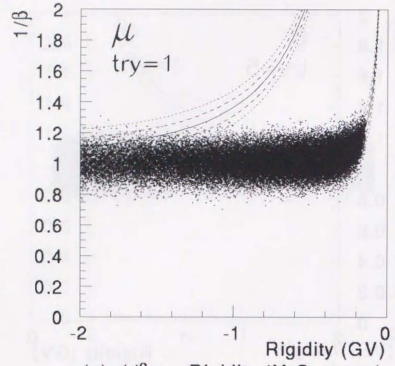

(a) 1/β vs. Rigidity (M.C. muon)

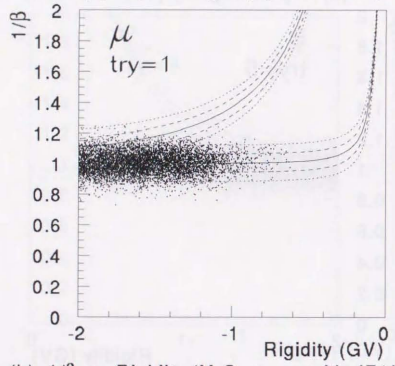

(b) 1/β vs. Rigidity (M.C. muon with dE/dX cut)

Figure 5.14: β^- vs rigidity for M.C. electron (a) before $\mathrm{d}E/\mathrm{d}X$ cuts and (b) after $\mathrm{d}E/\mathrm{d}X$ cut – Try-1.

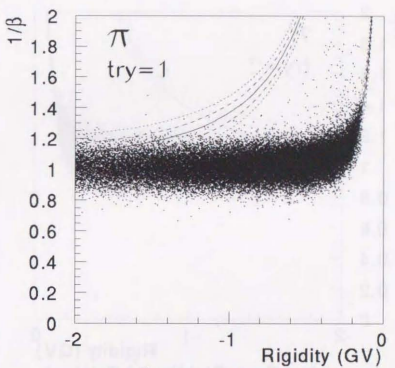

(a) 1/β vs. Rigidity (M.C. pion)

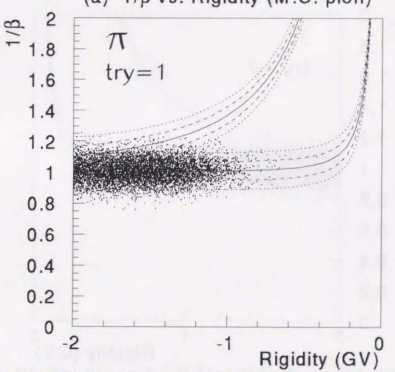

(b) 1/β vs. Rigidity (M.C. pion with dE/dX cut)

Figure 5.14: β^- vs rigidity for M.C. electron (a) before $\mathrm{d}E/\mathrm{d}X$ cuts and (b) after $\mathrm{d}E/\mathrm{d}X$ cut – Try-1.

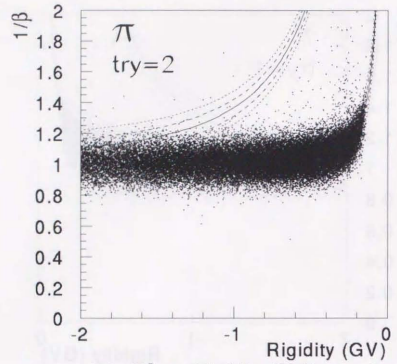

(a) 1/β vs. Rigidity (M.C. pion)

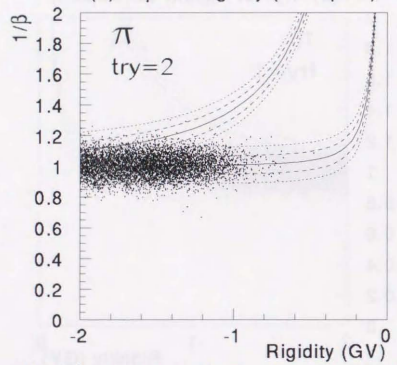

(b) 1/β vs. Rigidity (M.C. pion with dE/dX cut)

Figure 5.14: β^- vs rigidity for M.C. electron (a) before $\mathrm{d}E/\mathrm{d}X$ cuts and (b) after $\mathrm{d}E/\mathrm{d}X$ cut – Try-2.

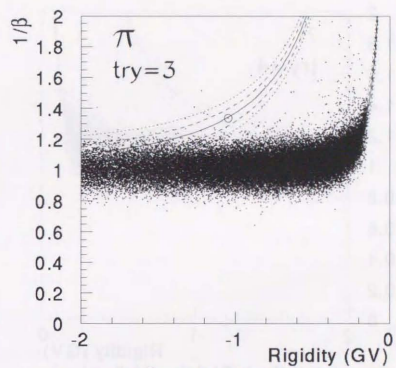

(a) 1/β vs. Rigidity (M.C. pion)

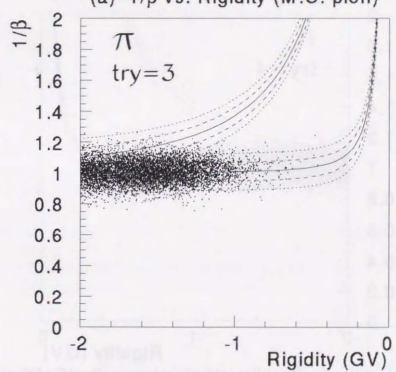

(b) 1/β vs. Rigidity (M.C. pion with dE/dX cut)

Figure 5.14: β^- vs rigidity for M.C. electron (a) before $\mathrm{d}E/\mathrm{d}X$ cuts and (b) after $\mathrm{d}E/\mathrm{d}X$ cut – Try-3.

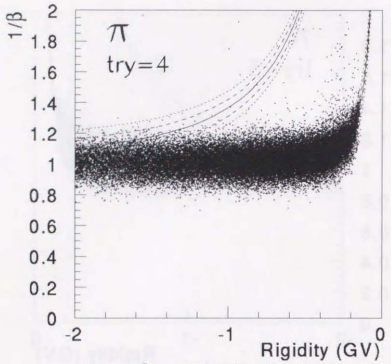

(a) 1/β vs. Rigidity (M.C. pion)

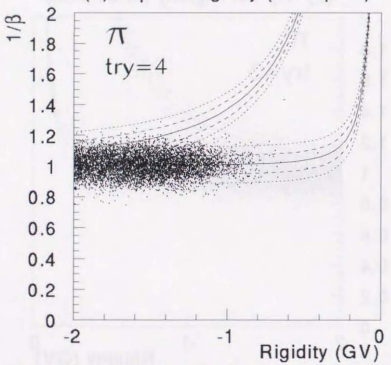

(b) 1/β vs. Rigidity (M.C. pion with dE/dX cut)

Figure 5.14: β^- vs rigidity for M.C. electron (a) before $\mathrm{d}E/\mathrm{d}X$ cuts and (b) after $\mathrm{d}E/\mathrm{d}X$ cut – Try-4.

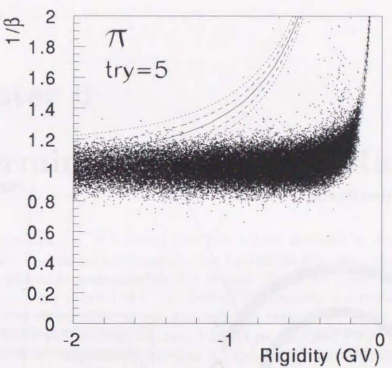

(a) 1/β vs. Rigidity (M.C. pion)

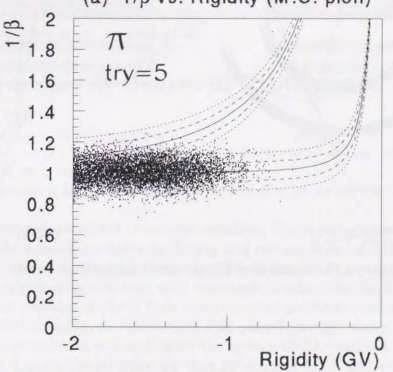

(b) 1/β vs. Rigidity (M.C. pion with dE/dX cut)

Figure 5.14: β^- vs rigidity for M.C. electron (a) before $\mathrm{d}E/\mathrm{d}X$ cuts and (b) after $\mathrm{d}E/\mathrm{d}X$ cut – Try-5.

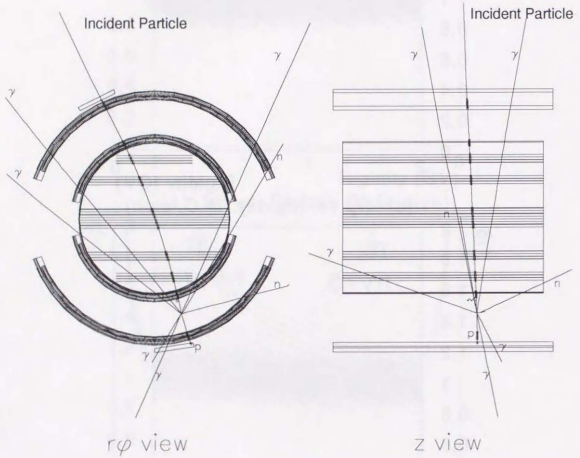

Figure 5.15: Example of the potential background event.

Chapter 6

Determination of the $\bar{p}/p$ Ratio

In the previous chapter, it is shown that four $\bar{p}$'s are detected in the rigidity region below 1 GV. To interpret this result, the equivalent $\bar{p}/p$ ratio at the top of the atmosphere (TOA) is determined in this chapter. First, the number of the observed protons and $\bar{p}$'s are counted in § 6.1. Section 6.2 presents a correction method for the energy loss of particles in the atmosphere. Section 6.3 and 6.4 describe the efficiencies which are necessary to correct loss of protons and $\bar{p}$'s in the detector and in the atmosphere, respectively. Section 6.5 discusses about secondary production of protons and $\bar{p}$'s by the primary cosmic-ray collision. In § 6.6, the $\bar{p}/p$ ratio at the TOA is calculated using parameters obtained in the above section. In the last section, systematic errors are evaluated.

6.1 Number of Observed Protons and Antiprotons

In the search for $\bar{p}$'s, we applied the various trigger- and off-line selections to the event data as described in the previous chapter.

Before counting the number of protons and $\bar{p}$'s, let us review these selections briefly.

There were three stages in the trigger selection. The first stage was the T0 trigger which was the coincidence between the top and bottom layers of TOF scintillators. The second stage was the hit-pattern selection in the TT to reject multi or empty hit-pattern which is inconsistent with the single track. The third stage was the track-rigidity selection in the TT to reject most of positively curved events using IDC and ODC hit-patterns. The events that passed through above three stages of selections were recorded and undergone the further off-line analysis. In the off-line analysis, we applied the selection for thee good single track and subsequently the track quality cut and the cut for the good timing measurement. Finally to extract proton and $\bar{p}$ signals, the dE/dX-band cut and the mass range cut were applied.

We define here the "total number of observed protons and $\bar{p}$'s" (N_p and $N_{\bar{p}}$, respectively) as the number of the protons and $\bar{p}$'s that passed through the hit-pattern selection and would have survived all off-line selections, if they were not

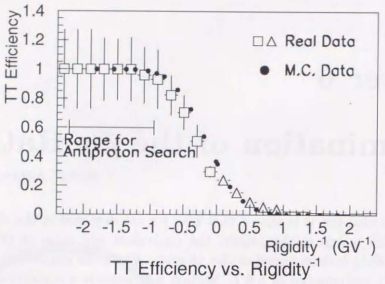

Figure 6.1: Track-rigidity selection efficiency

rejected by the track-rigidity selection. Simply, $N_{\bar{p}}$ and $\bar{N}_{\bar{p}}$ are the number of the protons and $\bar{p}$'s events, respectively, that passed through all selections but the track-rigidity selection.

The number $N_{\bar{p}}$ is obtained by counting events in the unbiased trigger sample that survived all of the trigger- and the selection-criteria except for the track-rigidity condition in the TT. Corrected by a factor 140, Np is found to be 1,178,800 in the rigidity range between 0.45 and 1.05 GV.

To calculate $\bar{N}_{\bar{p}}$ based on the four observed events, we have to correct for the small inefficiency in the rigidity selection of the track trigger. The efficiency are estimated both by using the negative muons/pions/electrons in the unbiased trigger sample and by the Monte Carlo simulation. Figure 6.1 summarizes the measured and simulated efficiency of the track-rigidity selection as a function of rigidity^{-1}. Boxes are the efficiencies measured using the unbiased samples of the negative muons/electrons/pions. Triangles are the efficiencies measured using protons. These measured efficiencies agree reasonably well with the results of the Monte Carlo simulation which are shown as the small points. In the region relevant to this $\bar{p}$ search, both the measured and the simulated efficiencies are close to 100%. We used the simulated efficiencies for the $\bar{p}$ counting.

6.2 Correction for Energy Loss

The observed protons and $\bar{p}$'s lost their energy while passing through the 5 g/cm^2-thick air and the detector. We have to correct the measured energy to get the energy at the TOA.

Suppose that the proton or $\bar{p}$ has a total energy E_0 at the TOA, the energy after passing material with the thickness of x g/cm^2, $E(x)$, is given by the following equation:

$$E(x) = E_0 - \int_0^x \frac{dE}{dx}(E(x))dx,$$

where $dE/dx(E(x))$ is the energy loss per unit material thickness as a function of the total energy. Differentiation of this equation gives

$$E'(x) = \frac{dE}{dx}(E(x)).$$

By solving this differential equation, the energy after passing through the material thickness can be obtained. The energy before loosing its energy can be also calculated in the same way from the material thickness which are estimated by extrapolating the track into the TOA.

From now on, we use the estimated kinetic energy at the TOA instead of rigidity in the calculation of efficiencies and fluxes. The rigidity range for $\bar{p}$'s decided in the previous chapter corresponds approximately to the kinetic energy range between 175 and 500 MeV at the TOA.

6.3 Instrumental Inefficiency

We then have to correct the loss of the particles in the instruments due to interaction with the material or due to the analysis selection. The following efficiencies of the selections, i.e., the probabilities of passing through the selections, should be determined for both protons and $\bar{p}$'s: (Variables with bar are for $\bar{p}$'s.)

- Efficiency of the good single track selection ($\varepsilon_{single}, \bar{\varepsilon}_{single}$).
- Efficiency of the hit-pattern selection in the TT ($\varepsilon_{TTpat}, \bar{\varepsilon}_{TTpat}$).
- Efficiency of the track quality cut ($\varepsilon_{TQ}, \bar{\varepsilon}_{TQ}$).
- Efficiency of the selection for the good timing measurement. ($\varepsilon_{TM}, \bar{\varepsilon}_{TM}$).
- Efficiency of the dE/dX-band cut ($\varepsilon_{band}, \bar{\varepsilon}_{band}$).
- Efficiency of the mass-range cut that define the proton and $\bar{p}$. ($\varepsilon_{mass}, \bar{\varepsilon}_{mass}$).

To determine these efficiencies, we utilized both the M.C simulation and the flight data as follows:

- In the M.C. simulation, protons and $\bar{p}$'s were isotropically injected to the instrument with various energies. The events were analyzed using the same analysis routine as the flight data.

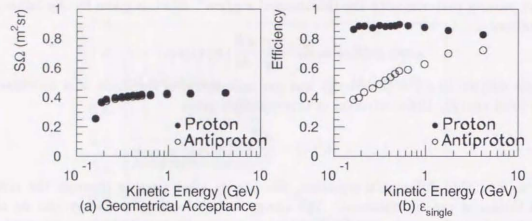

Figure 6.2: (a) Geometrical acceptance of BESS and (b) ε_{single} and $\bar{\varepsilon}_{single}$

- Unlike the M.C. data, since we have no information about the primary flux, we cannot determine ε_{single} from the flight data. We have to begin with extracting the proton events with a good single track. For this purpose, we applied loose cut on dE/dX and β as well as the good single track selection to extract protons without affecting other selections. Other efficiencies were determined from this proton sample.

Generally, the above efficiencies depend on the order in which they are applied since they are mutually correlated. In both cases, efficiencies were determined by applying the selections sequentially and then by counting the event number before and after the selections.

Before determining the efficiencies, we should first define the geometrical acceptance of the BESS detector using the good single track selection. We define it as the acceptance for passing through the BESS fiducial region without any interactions. This can be calculated by simulation with all interactions off and by counting the number of events that pass through the good single track selection. When interactions on, the loss due to the interactions is interpreted to $\varepsilon_{single}, \bar{\varepsilon}_{single}$. Figure 6.2 shows geometrical acceptance for protons and $\bar{p}$'s together with ε_{single} and $\bar{\varepsilon}_{single}$. The geometrical acceptance are almost identical for both protons and $\bar{p}$'s in the entire energy range, while ε_{single} and $\bar{\varepsilon}_{single}$ show significant difference in the low energies due to annihilation of $\bar{p}$'s.

Next, we determined all other efficiencies for protons by applying sequentially selection to the '93 flight data samples. Figure 6.3 shows the efficiencies calculated for protons. The relatively small efficiency of hit-pattern selection (ε_{TTpat}) is mainly due to the problem in the TT. The cross-talk in the IDC and ODC read-out electronics make hit-pattern dirty and results in the inefficiency of the hit-pattern selection.

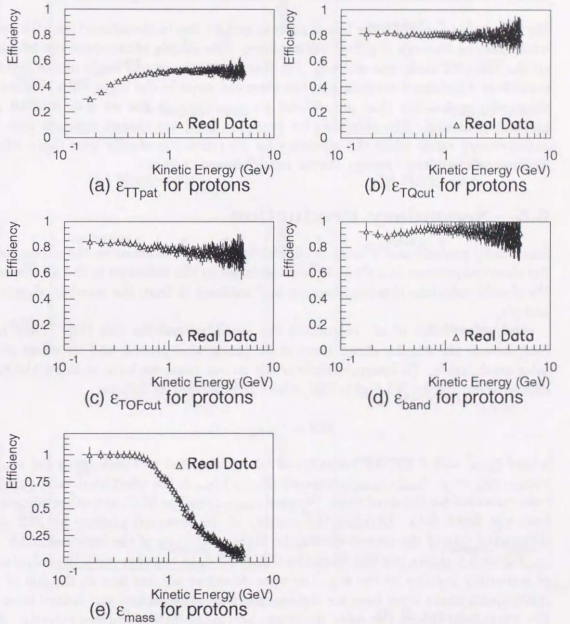

Figure 6.3: Efficiencies for protons

Finally, the ratio of the efficiencies for $\bar{p}$'s to those for protons were calculated using the M.C simulation data. Figure 6.4 summarizes the resultant efficiency ratios. The significant drop at low energies are due to annihilation of $\bar{p}$'s.

6.4 Interaction Loss in the Atmosphere

We then have to consider the loss of protons and $\bar{p}$'s due to the interaction with nuclei while passing through 5 g/cm^2 atmosphere. The simple atmosphere model based on the GEANT code was utilized. For this study, the zenith angle of the incident particle is distributed according to the observed angle in the flight data. Figure 6.5 shows the probability that proton and $\bar{p}$'s pass through the air slab without any inelastic collisions. The efficiency for protons (dots) are almost constant over the entire energy range while the efficiency for $\bar{p}$'s (circle) gradually goes down with a decrease of the kinetic energy due to annihilation.

6.5 Secondary Production

Since both protons and $\bar{p}$'s are produced by nuclear collisions in the atmosphere, the observed protons and $\bar{p}$'s include secondaries by the collisions in the atmosphere. We should calculate this contribution and subtract it from the number of protons and $\bar{p}$'s.

Recently Papini *et al.* calculated the secondary proton flux [42]. They took into account the angular dependence of the production process and the effect of the solar modulation. To interpret their result to our data, we have to know the total exposure during the '93 flight, $S\Omega t$, which is expressed as follows:

$$S\Omega t = S_{geom} \cdot \varepsilon \cdot t_{live},$$

where S_{geom} and ε are the geometrical acceptance and total efficiency ($\equiv \varepsilon_{single} \cdot \varepsilon_{TTpat} \cdot \varepsilon_{TQ} \cdot \varepsilon_{TF} \cdot \varepsilon_{band} \cdot \varepsilon_{mass}$), respectively, and t_{live} is the effective data acquisition time corrected for the dead time. We used ε_{single} from the M.C. and other efficiencies from the flight data. Dividing the number of the observed protons by $S\Omega t$ gives differential flux of the proton during the flight at the top of the instrument.

Figure 6.6 shows the flux from the BESS '93 data together with the calculation of secondary protons in the air. The open triangles are the flux at the top of the instrument, where error bars are statistical errors. The dashed and dotted lines are the secondary flux at the solar minimum and solar maximum, respectively. Also shown are the primary proton spectra calculated by force-field approximation [43] with various solar modulation parameters ($\phi = 500$ MV at the solar minimum and $\phi = 1000$ MV at the solar maximum). With these proton spectra the parameter for the BESS'93 flight is estimated to be 650 MV. If we take the secondary proton flux in the solar minimum, we can obtain the corrected data points (solid triangles) by subtracting the secondary contribution and subsequently correcting the efficiency in the air. They exhibit a reasonable agreement with two open squares which are

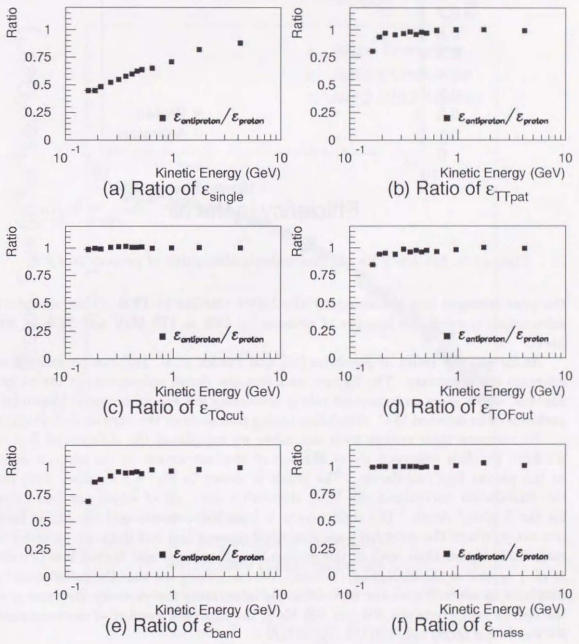

Figure 6.4: Ratio o efficiencies for anitprotons to those for protons.

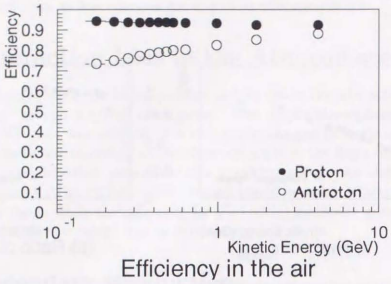

Figure 6.5: Efficiency for the atmospheric absorption of protons and $\bar{p}$'s.

the year-averaged flux measured by the IMP8 satellite in 1993. This secondary subtraction corrects the number of protons by 43% at 175 MeV and 91% at 500 MeV.

As for $\bar{p}$'s, the result of Stephens [44] and Pfeifer *et al.* [45] can be utilized to estimate the secondary. The former considers the Fermi momentum of the target nucleon, which plays an important role in producing low energy protons. Mitsui [46] performed the detailed M.C. simulation taking into account the angular distribution.

To compare their results with our data, we calculated the differential flux of $\bar{p}$'s from the four observed $\bar{p}$'s at the top of the instrument in the same manner as the proton flux calculation. The result is shown in Fig. 6.7 together with the two calculation curves and the M.C. simulation data, all of which are calculated for the 5 g/cm^2 depth. The right points is from three events and the left is from one event, where the error bars are statistical errors. The real data are an order of magnitude higher than both of the dashed line (Stephens) and dotted line (Pfeifer *et al.*) as well as the histogram (Mitsui). We can clearly see that the calculation by Stephens agrees well with the M.C data. By integrating the curve by Stephens over the energy range between 300 and 500 MeV, the expected number of the secondary $\bar{p}$'s was found to be 0.3.

It is still debatable whether the four $\bar{p}$'s had really come from the outside of the atmosphere since there remains the possibility that the secondary $\bar{p}$'s are produced in the thick layer of the atmosphere beneath the BESS detector. In such case, the trajectory of the $\bar{p}$ can be curved by the earth magnetic field and injected into the BESS detector as a reentrant down-going particle. To check this possibility, we trace back the trajectry of all $\bar{p}$'s using a Runge-Kutta method in the earth magnetic field and proved that they all have come from the outer space. Therefore we can conclude

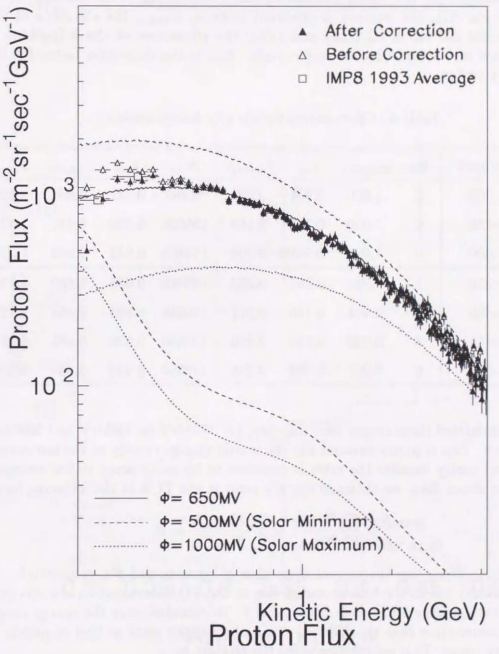

Figure 6.6: Comparison of the proton flux with the secondary proton flux due to collisions in the air.

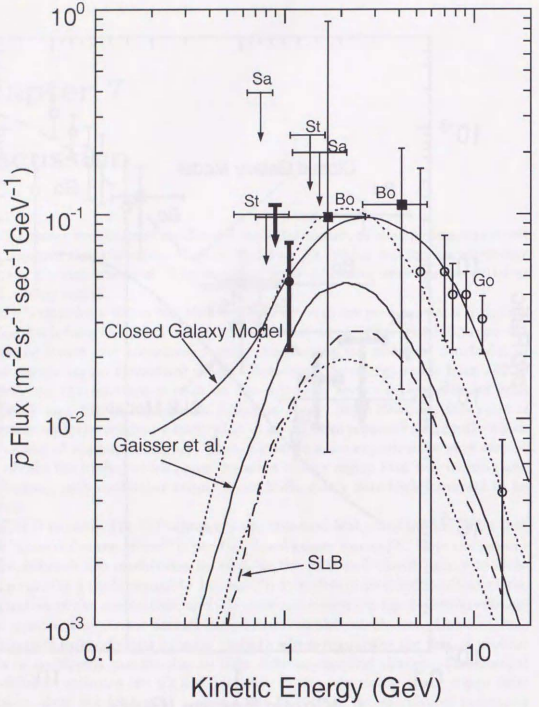

Figure 7.2: Comparison of the observed interstellar $\bar{p}$ flux with the other experimental and theoretical values. The BESS'93 data (bold lines) are demodulated with a solar modulation parameter of 650 MV. The curves labeled "SLB" and "Closed Galaxy Model" are from the calculation by Protheroe [2], being demodulated by Tan and Ng [48]. The solid and dotted curves are from Gaisser *et al.* [47]. The dotted curves represent the minimum and maximum errors.

propagation models.

Concerning the primordial black-hole (PBH), Maki *et al.* [41] recently employed the M.C. simulation to estimate the source strength and closely examine the propagation of $\bar{p}$'s in our Galaxy. In their calculation of $\bar{p}$ flux, they make no assumption concerning the mass distribution of a PBH. They define parameter ε_* as

$$\varepsilon_* \equiv \frac{M_*}{\rho_h}\frac{d\rho_0}{dM_0}(M_0 = M_*),$$

where ρ_0 is the density of a PBH within the Galactic halo with no Hawking radiation being assumed, ρ_h the density of the halo, and M_0 the initial mass a PBH at formation. The parameter ε_* is proportional to the present rate of PBH evaporation, and approximately indicates the mass density ratio of a PBH to the halo at $M_0 = M_*(\equiv 5.3 \times 10^{14}$ g) which should be at the final evaporating stage at present epoch.

Since the $\bar{p}$ flux from PBHs has a flat spectrum in the energy region below 1 GeV, it is reasonable to sum the whole data into one energy bin. A comparison of the resultant $\bar{p}/p$ ratio of $8.9 \pm 5 \times 10^{-5}$ with the above calculation enables a stringent upper limit (90% C.L.) to be set on ε_*, i.e.,

$$\varepsilon_* < 3.0 \times 10^{-8}\left(\frac{\rho_h}{0.3\ \mathrm{GeV\ cm^{-3}}}\right)^{-1}\left(\frac{M_*}{5.3 \times 10^{14}\mathrm{g}}\right)^2,$$

which corresponds an upper limit on the present rate of PBH evaporation, R, i.e.,

$$R < 8.1 \times 10^{-3} yr^{-1} pc^{-3}.$$

The PBH curve in Fig. 7.3 shows the results for $\varepsilon_* = 3 \times 10^{-8}$.

Based on this value of R, it is not likely that a γ-ray burst from a PBH can be detected, being independent of both ρ_h and M_*. In actuality, a recent null observation of a γ-ray burst with an energy above 50 TeV set R's upper limit as [49]:

$$R < 8.5 \times 10^5 yr^{-1} pc^{-3},$$

which is more than eight orders of magnitudes larger than that obtained from our data.

When a PBH is considered from a cosmological standpoint, this limit may infer a constraint on the density fluctuations occurring at early universe. According to the scenario that PBHs were formed from density inhomogeneities, those with mass M_* would be created at $t_* \simeq 10^{-23}$. If a flat Friedmann universe is assumed, we can calculate the fraction of the Universe's mass going into PBHs with mass M_*, $\beta(M_*)$, i.e.,

$$\beta(M_*) \simeq 1 \times 10^{-26}\left(\frac{\varepsilon_*}{10^{-8}}\right)\left(\frac{\Omega_h}{0.1}\right)\left(\frac{t_*}{10^{-23}\mathrm{s}}\right)^{-\frac{1}{2}}.$$

Therefore, applying the above upper limit on ε_* results in

$$\beta(M_*) < 3.0 \times 10^{-26}\left(\frac{\Omega_h}{0.1}\right)\left(\frac{t_*}{10^{-23}\mathrm{s}}\right)^{-\frac{1}{2}}\left(\frac{\rho_h}{0.3\mathrm{GeV\ cm^{-3}}}\right)^{-1}\left(\frac{M_*}{5.3 \times 10^{14}\mathrm{g}}\right)^2,$$

which corresponds to having the following upper limit on the amplitude of the density fluctuation, δ_H, i.e.,

$$\delta_H < 0.0317.$$

Combining this with δ_H observed by COBE [50] at mass region $M \sim 10^{55}$g, which is 40 orders of magnitude larger than the mass of a PBH, our upper limit on δ_H constrains the global shape of the density fluctuation spectrum.

If we assume that the density fluctuation is scale-invariant as predicted in many cosmological models including inflationary ones, the mass distribution of PBH can be predicted. The limit on ε_* (i.e., the limit on the present evaporating rate) can then be converted to an upper limit on an density parameter of PBHs, Ω_{PBH}, i.e.,

$$\begin{aligned} \Omega_{PBH} &\simeq 2.0 \times 10^{-9} \left(\frac{\varepsilon_*}{10^{-8}}\right) \left(\frac{\Omega_h}{0.1}\right) \\ &< 6.0 \times 10^{-9} \quad \text{for} \quad \Omega_h = 0.1. \end{aligned}$$

As such, although various uncertainties exist concerning the spatial distribution of PBHs and the employed propagation model, this is a stricter upper limit than that obtained by γ-ray background measurements, which is the most strict limit on Ω_{PBH}.

With regard to $\bar{p}$ production by neutralinos, Jungman and Kamionkowski [26] showed that a cosmic-ray $\bar{p}$ produced by the annihilation of neutralinos into a two-gluon final state is competitive with a tree-level annihilation process occurring in large parameter space. They calculated the $\bar{p}$ spectrum by mainly assuming the pure B-ino state to be the WIMP constituent. In their calculation, the $\bar{p}$ spectrum at the boundary of our Galaxy, $\phi_{\bar{p}}^{is}(E)$, is written as

$$\phi_{\bar{p}}^{is}(E) = \frac{1}{4\pi} c\tau_{esc}(E) q_{\bar{p}}(E)$$

where E is the energy of a $\bar{p}$, $\tau_{esc}(E)$ the energy-dependent confinement time, and $q_{\bar{p}}(E)$ the $\bar{p}$ source function defined as the differential number of $\bar{p}$'s produced per unit volume, time interval, and energy interval. If $\tau_{esc} = 10^8$ yrs, then the obtained $\bar{p}/p$ ratio is as shown in Fig. 7.3. The "30-GeV B-ino" curve indicates the expected spectrum if a 30-GeV B-ino populates the Galactic halo. Even though the BESS $\bar{p}$ flux ratio for both energy bins is compatible with their calculated flux, this does not necessarily confirm the possible existence of neutralinos nor place stringent limits on certain parameters, since astrophysical uncertainties exist concerning the source density, confinement time, and neutralino mass. In addition, the lack of knowledge about secondary $\bar{p}$'s makes confirmation difficult, though higher statistics would probably help. Jungman and Kamionkowski [26] suggested that the neutralino to $\bar{p}$ channel is complimentary to the energetic neutrino channel since the $\bar{p}$ signal is likely to be enhanced, whereas the neutrino signal is likely to be depleted.

It should be realized that in any case more data is needed to further invstigate the physics concerning cosmic-ray $\bar{p}$'s. An extention of the energy range for measuring $\bar{p}$'s is also important to determine the $\bar{p}$ spectral shape, which is a key information to distinguish the various physical models producing $\bar{p}$'s. We plan a long-duration

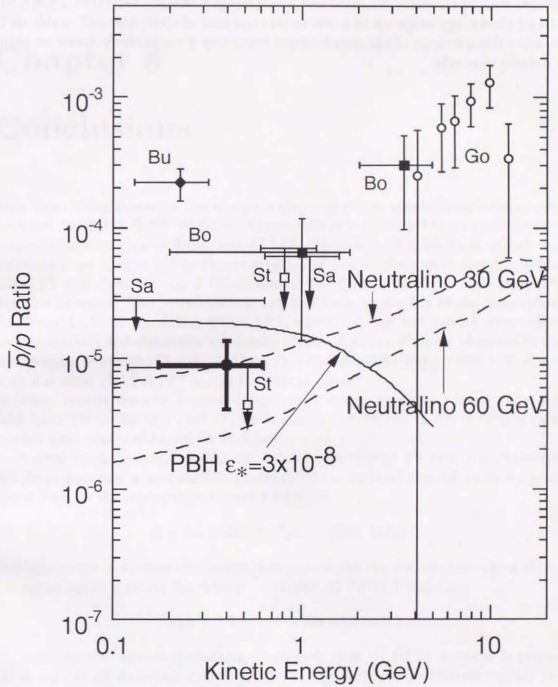

Figure 7.3: Comparison of the BESS '93 result with other theoretical models. The BESS'93 data are combined into one bins. Data symbols are same as Fig.1.1. The PBH curve represents the expected value for $\varepsilon_* = 3 \times 10^{-8}$, corresponding to the upper limit from the BESS '93 data.

flight of up to 15 days, which will provide the data with an order of magnitude higher statistics than the present data. Besides, addition of particle identification devices such as Čerenkov counters and a ring image Čerenkov detector (RICH), will extend the energy range up to a few to serveral tens of GeV, and will enable us to measure the spectrum of the cosmic-origin secondary $\bar{p}$'s accurately, based on many hundreds of events.

Chapter 8

Conclusions

This dissertation described low-energy cosmic-ray $\bar{p}$ flux measurements using data recorded during the BESS '93 flight. Antiprotons were identified by measurements of magnetic rigidity, time of flight, and dE/dX. The resultant good track quality and sufficient mass spectra led to the observation of four of the lowest-energy, cosmic-origin $\bar{p}$'s ever observed, all of which showed the correct TOF and were separated from background. The corresponding $\bar{p}/p$ flux ratio at the top of the atmosphere was found to be $(1.2 \pm 0.65 \pm 0.2) \times 10^{-5}$, where the first and second error values are respectively statistical and systematic errors. Since no $\bar{p}$'s were observed in the energy range between 175 and 300 MeV, this enables establishing a 90% C.L. upper limit flux ratio of 2.9×10^{-5} across the energy range.

These results are new because (i) no one has ever reported a finite value $\bar{p}/p$ ratio from 300 to 500 MeV, and (ii) the upper limit from 175 to 300 MeV is in clear conflict with results obtained by Buffington *et al.*

Several novel mechanisms that can produce low-energy $\bar{p}$'s were also discussed. For the evaporating primordial black holes (PBHs), our results can place an stringent upper limit on the evaporation rate of a PBH, R, i.e.,

$$R < 8.1 \times 10^{-3} yr^{-1} pc^{-3} \quad (90\% \text{ C.L.})$$

In addition, use of a reasonable assumption concerning the density fluctuation allows setting an upper limit on the density parameter of PBHs, Ω_{PBH}, i.e.,

$$\Omega_{PBH} < 6.0 \times 10^{-9} \quad for \quad \Omega_h = 0.1$$

Based on the presented analysis, I conclude that (i) BESS detector is proved to be capable of detecting cosmic-ray $\bar{p}$'s in the hetherto-unobserved region, (ii) The observed $\bar{p}$ flux shows the low-background feature at low energies as suggested by the theoretical calculation, and (iii) to further elucidate the physics relevant to cosmic-ray $\bar{p}$'s, data is required with higher statistics in both low-energy (< 1 GeV) and high-energy (≥ 1 GeV) region.

References

[1] T.K. Gaisser, and R.H. Maurer, Phys. Rev. Lett. **30**, 1264 (1979).

[2] R. J. Protheroe, Astrophys. J. **251**, 387 (1981).

[3] H. Aizu et al., Phys. Rev. **121**, 1206 (1961).

[4] M. V. K. Apparao, Nature **215**, 727 (1967).

[5] R. L. Golden et al., Phys. Rev. Lett. **43**, 1196 (1979).

[6] E.A. Bogomolov, et al., Proc. 20th Intern. Cosmic Ray Conf. (Moscow), **2**, 72 (1987).

[7] E.A. Bogomolov, et al., Proc. 21th Intern. Cosmic Ray Conf. (Adelaide), **3**, 288 (1990).

[8] A. Buffington, S. M. Schindler, and C. R. Pennypacker, Ap. J.**248**, (1981) 1179.

[9] M. H. Salamon et al., Ap. J. **349**, 78 (1990).

[10] S. J. Stochaj, Ph.D. thesis, Univ. of Maryland, (1990)

[11] A. Moas *et al.* , Proc.. 21st Intern. Cosmic Ray Conf. (Adelaide), **3**, 284 (1990).

[12] J. Audouze and C. J. Cesarsky Nature Phys. Sci. **214**, 98 (1973).

[13] I. L. Rasmussen and B. Peters, Nature **258**, 412 (1975).

[14] B. Peters and N. J. Westergaad, Ap. Space Sci. **48**, 21 (1977).

[15] L. C. Tan and L. K. Ng, J. Phys. G, Nucl. Phys. **9**, 227 (1983).

[16] C. J. Cesarsky and T. M. Montmerle, Proc. 17th Internat. Cosmic Ray Conf. (Paris, France), **9**, 207 (1981).

[17] R. Cowsik and T. K. Gaisser, Proc. 17th Internat. Cosmic Ray Conf. (Paris, France), **2**, 218 (1981).

[18] V. L. Ginzburg and V. S. Ptukin, Sov. Astro Lett. **7**, 325 (1981).

[19] S. A. Stephens and B. G. Mauger, Ap. Space Sci. **110**, 337 (1985).

[20] C. D. Dermer and R. Ramaty, Nature **319**, 205 (1986).

[21] J. Silk and M. Srednicki, Phys. Rev. Lett. **53**, 624 (1984).

[22] F. W. Stecker and A. W. Wolfendale, Nature **309**, 37 (1984).

[23] J. S. Hagelin and G. L. Kane, Nucl. Phys. B **B263**, 399 (1986).

[24] F. W. Stecker, S. Rudaz, and T. F. Walsh, Phys. Rev. Lett. **55**, 2622 (1985).

[25] S. Rudaz and F. W. Stecker, Ap. J. **325**, 16 (1988).

[26] G. Jungman, M. Kamionkowski, Phys. Rev. D **D49**, 2316 (1994).

[27] S. W. Hawking, Nature **248**, 30 (1974).

[28] P. Kiraly, J. Wdowczyk, and A. W. Wolfendale, Nature **293**, 120 (1981); M.S. Turner, Nature **297**, 379 (1982).

[29] R. W. Brown and F. W. Stecker, Phys. Rev. Lett. **43**, 315 (1979).

[30] K. Sato, Phys. Lett. **B99**, 66 (1981).

[31] F. W. Stecker, Nuc. Phys. **B252**, 25 (1985).

[32] F. W. Stecker and A. W. Wolfendale, Nature **309** 37 (1984).

[33] V. Trimble, Ann. Rev. Astr. Ap. **25**, 425 (1987).

[34] J. Yang, et al., Ap. J. **281**, 493 (1984).

[35] D. J. Hegyi and K. A. Olive, Ap. J. **303**, 56 (1986).

[36] S. Rudaz and F. W. Stecker , Ap. J. **325**, 16 (1988).

[37] A. Yamamoto *et al.* , IEEE Trans. on Mgneetics **24**, 1421 (1988).

[38] M. Goossens *ZEBRA manual* (1991)

[39] M. Imori, et al. IEEE Transactions on Nuclear Science **39**, 1389

[40] V. Karimäki, Report of University of Helsinki, HU-SEFT-1991-10.

[41] K. Maki, T. Mitsui, and S. Orito, "Low-energy Antiproton Signiture of Evaporationg Primordial Black Holes", ICEPP-9403, 1994

[42] P. Papini, C. Grimani, S. A. Stephens. 22st Intern. Cosmic Ray Conf., eds. (Calgary, Canada, 1993)

[43] L. J. Glesonn and W. I. Axford, Ap. J. **154**, 1011 (1968).

[44] S. A. Stephens, Proc. 22st Intern. Cosmic Ray Conf., eds. (Calgary, Canada, 1993)

[45] Ch.Pfeifer, U. Heinbach and M. Simon, Proc. 22st Intern. Cosmic Ray Conf., eds. (Calgary, Canada, 1993)

[46] T. Mitui. private communication, 1994.

[47] T. K. Gaisser and R. K. Schaefer, Ap. J. **394**, 174 (1992).

[48] L. C. Tan and L. K. Ng, J. Phys. **G 9** 227, (1983).

[49] D. E. Alexandreas *et al.* , Phys. Rev. Lett. **71**, 2524 (1993).

[50] D. B. Cline and W. Hong, Ap. J. **436**, 423 (1992).